Dhx38 regulates the maintenance and differentiation of erythro-myeloid progenitors and hematopoietic stem cells by alternative splicing

Jiayi Tu[1,*], Shanshan Yu[2,*], Jingzhen Li[1], Mengmeng Ren[1], Yangjun Zhang[3], Jiong Luo[1], Kui Sun[1], Yuexia Lv[1], Yunqiao Han[1], Yuwen Huang[1], Xiang Ren[1], Tao Jiang[1], Zhaohui Tang[1], Mark Thomas Shaw Williams[4], Qunwei Lu[1,‡], Mugen Liu[1,‡]

[1]Key Laboratory of Molecular Biophysics of Ministry of Education, College of Life Science and Technology, Huazhong University of Science and Technology, Wuhan, 430074, P.R. China

[2]Institute of Visual Neuroscience and Stem Cell Engineering, College of Life Sciences and Health, Wuhan University of Science and Technology, Wuhan, Hubei, P.R. China

[3]Tongji Hospital, Tongji Medical College, Huazhong University of Science and Technology, Wuhan, 430030, P.R. China

[4]Charles Oakley Laboratories, Department of Biological and Biomedical Sciences, Glasgow Caledonian University, Glasgow, G4 0BA UK

[*]co-first authors

[‡]Corresponding author: Mugen Liu, lium@mail.hust.edu.cn

Qunwei Lu, Email: luqw@hust.edu.cn.

Summary statement

Fetal hematopoietic processes include the erythroid-myeloid progenitor process and the hematopoietic stem cell process. Splicing factor dhx38 governs both processes by regulating the splicing of cell cycle genes.

Abstract

Mutations that occur in RNA splicing machinery may contribute to hematopoietic-related diseases. How splicing factor mutants perturb hematopoiesis, especially in the erythro-myeloid progenitors (EMP) process, remains elusive. Dhx38, a pre-mRNA splicing-related DEAH box RNA helicase, whose physiological function and splicing mechanisms during hematopoiesis currently remain unclear. Here we present that Dhx38 exerts a broad effect on definitive EMPs as well as the differentiation and maintenance of hematopoietic stem and progenitor cells (HSPCs). In *dhx38* knockout zebrafish, EMPs and HSPCs are found arrested in mitotic prometaphase, accompanied by a 'grape' karyotype, due to the defects in chromosome alignment. Abnormal alternative spliced genes related to chromosome segregation, microtubule cytoskeleton, cell cycle kinase, and DNA damage are present in the *dhx38* mutants. Subsequently, their EMPs and HSPCs undergo *p53*-dependent apoptosis. This study provides novel insights into alternative splicing regulated by Dhx38, a process that plays a critical role in proliferation and differentiation of fetal EMPs and HSPCs.

Introduction

Alternative splicing is a fundamental regulatory mechanism of the gene expression process in higher organisms, requiring accurate regulation of RNA-splicing machinery (Baralle and Giudice, 2017). The early-onset of mutations in components of RNA-splicing machinery is present in >50% of myelodysplastic syndrome (MDS) patients, and nearly 60% of genes were predicted to undergo alternative splicing during human hematopoiesis (Chen et al., 2014). Emerging data show that splicing factor mutants, to some degree, define distinct clinical phenotypes and often have different prognostic impacts (Pellagatti and Boultwood, 2020). Understanding the diversity and complexity of alternative splicing in hematopoiesis remains a challenge.

Hematopoiesis is a hierarchical system, in which hematopoietic stem and progenitor cells (HSPCs) differentiate into progressively committed progenitors and mature cells (Mitroulis et al., 2018). HSPCs maintain self-renewal and multilineage blood differentiation with a sophisticated mechanism to provide lifelong hematopoiesis. Dysplasia of HSPCs is frequently associated with an increased risk of hematopoietic-related diseases, such as MDS and acute myeloid leukemia (Baeten and de Jong). Before the emergence of HSPCs, lineage-restricted progenitors, such as erythro-myeloid progenitors appear and overlap with the latter half of primitive hematopoiesis and the emergence of HSPCs from the dorsal aorta at 36 to 48 hpf (Da'as et al., 2012). EMPs give rise to fetal erythrocytes, myeloid lineages, natural killer cells, adult tissue-resident macrophages, and can be distinguished via the expression of *lmo2* and *gata1* (Dege et al., 2020; Li et al., 2018b). Compromised EMPs impair the formation of fetal erythrocytes, and adult macrophages, resulting in fetal hemoglobinopathy, late-onset neurodegeneration, or chronic inflammatory diseases (Hoeffel et al., 2015; Mass et al., 2017; McGrath et al., 2011). Whilst several studies have been carried out to demonstrate the role of splicing factors in hematopoietic development, up until now, few studies have found the role of splicing factors in EMP defects.

EMPs and HSPCs both emerge from hemogenic endothelium and differentiate into multiple blood cells. In this process, they share common and also distinct mechanisms of development (Yokomizo et al., 2018). For example, canonical Wnt signaling is a common mechanism regulating the emergence of EMPs and HSPCs (Frame et al., 2016). But distinct from HSPCs, EMPs do not require Notch signaling during their appearance (Bertrand et al., 2010). Dysfunction of the HSPC process has been observed in splicing factor knockout models, such as Sf3b1, Ddx41, U2af1, etc (Danilova et al., 2010; De La Garza et al., 2016; Weinreb et al., 2021). However, the mechanism by which splicing factors regulate both EMP and HSPC processes still required to be fully determined.

*Dhx*38 encodes the RNA helicase PRP16 and is required to destabilize the U2-U6 helix I between the splicing pathway's first and second catalytic steps (Fica et al., 2017). Dhx38 is the only RNA helicase that binds to mitotic noncoding RNA, and interference with *dhx38* affects mitotic function and leads to disrupted chromatin arrangement during the mitotic M phase (Nishimura et al., 2019). In fission yeast, mutations of *dhx38* affect a small subset of introns with weak 5'SS-U6 snRNA interactions (Vijayakumari et al., 2019). DHX38 is an endogenous inhibitor of the protein phosphatase PP4, which regulates DNA damage repair and microtubule development (Han et al., 2015). Missense mutations in *dhx38* affect the splicing of cell cycle-related genes and regulate heterochromatinization of centromere. Latif *et al.* identified that the missense variant c.971G > A of *dhx38* is involved in the early-onset etiology of retinitis pigmentosa (Latif et al., 2018). However, there are no theoretical or experimental reports so far regarding the regulation of DHX38 in the hematopoietic system. We found that high expression of DHX38 was restricted to the lymphoid neoplasm diffuse large B-cell lymphoma (DLBC) and also thymoma (THYM) in the GEPIA database, and in 2006, DHX38 was reported to be amplified in AML (Ma et al., 2006). Whether and how DHX38 acts in the hematopoietic system needs to be further explored.

Zebrafish is an ideal model for investigating embryonic hematopoiesis study, since it can survive for several days independently of the cardiovascular system (Li et al., 2018a). Here we constructed a *dhx38* knockout zebrafish line, and observed its hematopoietic

development during embryogenesis. Our study highlights the physiological function and splicing mechanisms of Dhx38 during hematopoiesis, and also demonstrates its role in regulating both EMPs and HSPCs.

Results

Dhx38 is highly expressed in the hematopoietic region

To establish the expression pattern of *dhx38* in zebrafish embryos, we performed a whole-mount in situ hybridization (WISH) via the *dhx38* probe. We observed that the expression of *dhx38* is ubiquitously expressed throughout the zebrafish embryos. Outside of the head and tail, we also identified high expression of *dhx38* in the posterior blood island (PBI) at 36 hpf (hours-postfertilization), and in caudal hematopoietic tissue (CHT) at 48 hpf, where erythro-myeloid progenitors (EMPs) and hematopoietic stem cells (HSPCs) are known to colonize (Fig. S1A). Moreover, the *dhx38* promoter drives mCherry expression in the PBI at 36 hpf and co-localizes with *cmyb*, a marker of EMPs and HSPCs (Bertrand et al., 2008; Hoeffel et al., 2015) (Fig. 1A-B). These data imply that the expression of *dhx38* is potentially required for the development of EMPs and HSPCs. We generated a *dhx38*$^{-/-}$ zebrafish line using CRISPR/Cas9 technology (Fig. 1C), with a 10 bp deletion in *dhx38* cDNA (c.11_21delTTCCTCCCTG), which was predicted to generate a truncated protein (p.Ser5_ThrfsTer7) (Fig. 1D). The mRNA level of *dhx38* is undetectable in the *dhx38*$^{-/-}$ embryo at 36 hpf (Fig. 1E).

EMP differentiation is blocked in *dhx38*$^{-/-}$ zebrafish

Primitive hematopoiesis occurs as an early but transitory wave, generating primitive erythrocytes and macrophages at 12-26 hpf. Myeloid progenitor marker *pu.1*, erythroid progenitor marker *gata1* and hemangioblasts marker *scl* are typically expressed in lateral plate mesoderm of *dhx38* mutants at 13 hpf (Fig. S1B). The expression of myelocyte marke*r mpx* and *lyz in rostral bl*ood island, and the erythrocytes marker *β-e-globin* in

intermediate cell mass, show no difference between wild-type siblings and *dhx38* mutants at 24 hpf (Fig. S1C). Primitive hematopoiesis is unaffected in the *dhx38*$^{-/-}$ zebrafish.

HSPCs originate from arterial endothelium. The arterial marker *dll4* and venous marker *dab2* at 36 hpf show no significant difference between *dhx38*$^{-/-}$ embryos and siblings (Fig. S1D). Also, the patterns of dorsal aorta (DA), posterior cardinal vein (PCV), caudal artery (CA), caudal venous plexus (CVP), and intersegmental vessels (ISV) indicate well-developed angiogenesis in *dhx38*$^{-/-}$;Tg (*flk1*:mCherry) at 36 hpf and 48 hpf (Fig. S1E). These data suggest that the development of the vasculature appears to be unaffected in the *dhx38* mutants.

Definitive hematopoiesis initiates through committed EMPs in the PBI that arise independently from HSPCs at 30-36 hpf (Bertrand et al., 2007). EMPs can differentiate into multiple lineages of blood cells, including erythrocytes, macrophages, granulocytes, and mast cells, and are labeled by *gata1*$^{+}$/*lmo2*$^{+}$ double-positive cells (Bertrand et al., 2010). The expression of *lmo2* and *gata1* (EMPs) is normal at 30 hpf (Fig. S2A), but dramatically increases at 33 hpf in the PBI of *dhx38* mutants (Fig. 1F, J). We further examined the expression of genes downstream of EMPs differentiation, including *pu.1* and *cebpa* (promyelocytes), which are highly expressed in immature cells, and within undifferentiated myeloid cells in some hematopoietic cancer (Dai et al., 2016). Both cell types are expressed normally in the PBI of the *dhx38* mutant at 30 hpf (Fig. S2B), with expression increasing at 33 hpf (Fig. 1G, J), suggesting a crucial role of Dhx38 in mediating EMP development.

We investigated the expression of *mpx*, *mfap4*, *mpeg1.1* and *hbae1*, markers for mature granulocytes, mature macrophages and mature erythrocytes respectively, in the *dhx38* siblings and mutants. The mRNA profiles are almost identical in their PBI at 30 hpf (Fig. S2C), but decrease at 33 hpf and 36 hpf in the mutants (Fig. 1H-I, J, Fig. S3B). These results were confirmed by qRT-PCR (Fig. S3C). The increased immature blood cells and decreased mature blood cells are characteristic of a block in EMP differentiation.

Bertrand *et al.* isolated EMPs using *lmo2⁺gata1⁺* zebrafish at 30 hpf, and validated the tracing of EMP cells by using *cmyb⁺* and *gata1⁺* (Bertrand et al., 2010; Forrester et al., 2012). Consistent with our WISH results, the number of *gata1⁺cmyb⁺* cells and *pu.1⁺* cells in the PBI region of *dhx38* mutants are significantly increased as compared to wildtype siblings at 36 hpf and 48 hpf, suggesting the accumulation of immature EMPs and promyelocytes in the *dhx38* mutants (Fig. 2A-B, I-J, Fig. S3A).

We then employed a zebrafish line, Tg(*mpeg1⁺*:eGFP) trace developing macrophages. Mature *mpeg1⁺* cells display typical branched morphology in the PBI of wildtype siblings, but fewer branched mature macrophages in the PBI of *dhx38* mutant at 48 hpf (Fig. 2C, I). Granulocytes identified by Tg(*mpx*:eGFP) are also significantly reduced in the mutants (Fig. 2D, J). Taken together, these results suggest that EMP maturation is impaired in the *dhx38⁻ᐟ⁻* embryo. Embryos stained by Sudan Black show a lower number and smaller granulocyte size, representing immature granulocytes, in *dhx38⁻ᐟ⁻* embryos than in wild-type siblings (Fig. 2E, K). The phagocytic macrophages stained with a neutral red show that the functional macrophages in the PBI of *dhx38* mutant are significantly reduced (Fig. 2F, L). The increase in immature blood cells and the reduction of mature blood cells clearly show that EMP differentiation is blocked in the *dhx38⁻ᐟ⁻* embryo.

Loss of *dhx38* impairs definitive HSPC development.

Similar to mammals, definitive hematopoiesis in zebrafish is divided into two independent stages, EMP development and HSPC development. WISH and fluorescent microscopy were employed to investigate whether loss of Dhx38 affects the development of definitive HSPCs in embryos. HSPCs labeled by a *cmyb* probe are correctly identified and localized in the VDA of *dhx38* mutants at 36 hpf. Moreover, HSPCs in the *dhx38* mutants are found to be higher number compared to that of their wildtype counterparts at 48 hpf, but this increase disappears completely at 56 hpf (Fig. S3D). Fluorescence microscopic observation on *dhx38⁻ᐟ⁻*;Tg(*flk*:mCherry;*cmyb*:eGFP) fish reveal that the formation of hematogenic endothelium (*flk⁺*;*cmyb⁺*) is comparable with wild-type siblings in the VDA at

36 hpf. HSPCs accumulated in the CHT at 48 hpf, but then subsequently decreased to 56 hpf in the CHT (Fig. 3A). The emergence of HSPCs is normal while HSPC maintenance is perturbed in the *dhx38* mutants.

Given the impaired maintenance of HSPCs in *dhx38* mutant at 56 hpf, we examined the differentiation of HSPCs. Unsurprisingly, the *dhx38*^{-/-} embryos lacked the expression of the myeloid marker *lyz*, the erythroid marker *α-globin* in the CHT at 3 dpf, and the lymphoid mark *rag1* in the thymus at 4 dpf (Fig. S3E). Defects in HSPC maintenance, in the *dhx38* mutants, further resulted in a complete loss of lifelong hematopoiesis.

It seems EMPs overlap with the HSPCs in the PBI region from at 30 to 40 hpf, but can be labeled based on *cd41*[+]*gata1*[+] (EMPs) and *cd41*[+]*gata1*[-] (HSPCs) markers respectively as previously reported (Bertrand et al., 2010; Bertrand et al., 2008; Forrester et al., 2012; Xia et al., 2021). We then distinguished HSPCs from EMPs by *cmyb* and *gata1* markers in the PBI region. Both *cmyb*[+]*gata1*[+] and *cmyb*[+]*gata1*^{-} cells were increased at 48 hpf, but decreased rapidly at 56 hpf in the *dhx38*^{-/-} embryos (Fig. 3B-E), indicating that EMPs and HSPCs share similar dynamic characteristics, accumulating at first and then decreasing at later stages. Using an F0 strain, *dhx38* del7 (c.14_21delCTCCCTG), we also confirm the role of dhx38 in hematopoiesis, as this mutant phenocopies that of the *dhx38* del10 mutant confirming (Fig. S9).

Dhx38 deficiency induces abnormal cell cycle and apoptosis of EMPs and HSPCs.

To further interrogate the biological basis by which EMPs and HSPCs accumulate in the *dhx38* mutants, we examined their proliferation. 5-Ethynyl-2'-deoxyuridine (EdU) experiments revealed that cells undergoing S-phase within 2 h, are significantly reduced in the PBI of *dhx38*^{-/-} embryo at 36 hpf (Fig. 4A-D). In contrast, immunofluorescence of phosphorylated histone H3 (pH3) shows both cell types are arrested at M-phase in the PBI of *dhx38* mutants at 36 hpf (Fig. 4E-H). Meanwhile, pH3^{+} positive cells exhibit an abnormal chromosome karyotype in *dhx38*^{-/-} embryos (Fig. S4A). Interference of DHX38

in K562 leukemia cells phenocopies the G2/M arrest observed in the *dhx38* mutants (Fig. 4I; Fig. S4B). We hypothesized that the cell cycles of EMPs and HSPCs are arrested at M phase in *dhx38*$^{-/-}$ embryos. Moreover, an enhanced DNA damage signal is observed in the *dhx38* mutants at 36hpf and 56 hpf, indicating impaired cell cycle (Fig. 4J).

The numbers of EMPs and HSPCs are decreased in *dhx38*$^{-/-}$ embryos at 56 hpf. We therefore evaluated apoptosis of EMPs and HSPCs in *dhx38*$^{-/-}$ embryos, via the TUNEL assay. Although there is no significant difference between *dhx38* mutants and wild-type siblings, with regards to the proportion of apoptotic EMPs at 36 hpf in the PBI (Fig. S4C, D), apoptosis increased significantly in the PBI of *dhx38*$^{-/-}$ embryos at 56 hpf (Fig. 4K-N). Also, inhibiting p53 activity in *dhx38* mutants failed to rescue the phenotype of granulocyte (*mpx*) and erythrocyte (*hbae3*) reduction at 36 hpf (Figure 8C; Figure S4E). Therefore, we eliminate the possibility that the changes in granulocyte and erythrocyte numbers in *dhx38* mutants at 36 hpf are due to defects in the viability of differentiated cells. But It strongly suggests that the observed reduced number of EMPs and HSPCs at 56 hpf are the result of increased apoptosis.

We then performed a more detailed investigation of mitosis by mointer the statue of chromosome and spindle during mitosis in the *dhx38*$^{-/-}$ embryos. A wide range of EMPs and HSPCs, exhibited karyotypic abnormalities in the PBI of the *dhx38*$^{-/-}$ zebrafish at 36 hpf and 48 hpf (Fig. 5A-B). In metaphase, EMPs and HSPCs in wild-type siblings exhibited typical chromosome alignment on the equatorial plane, with spindles attached to the centromeres, while EMPs and HSPCs in the *dhx38* mutants displayed an increase in the impaired alignment of chromosomes. Intriguingly, a previous study found a similar chromatin phenotype, called the 'grape' phenotype, when DHX38 was depleted from HeLa cells (Nishimura et al., 2019). In anaphase, the *dhx38* mutants exhibited an abnormal chromatin phenotype accompanied by a progressively abnormal spindle morphology (Fig. 5C-F, Fig. S5).

Lack of *dhx38* results in abnormal alternative splicing in cell cycle-related genes

We profiled the transcriptomes of the PBI region of wild-type siblings and mutants by RNA-seq at 36 hpf. This analysis revealed that 164 down-regulated genes and 386 up-regulated genes were mainly enriched in the centromere-related genes, and the P53 signaling pathway (Fig. S6A-C, Table. S1-2). These findings are consistent with the observation of abnormal mitosis and increased apoptosis in the *dhx38* mutants. Since *dhx38* mainly mediates the splicing process of pre-mRNA, we speculate that abnormal splicing events may be the cause of hematopoietic abnormalities. RNA-seq analysis revealed 150 intron-retained (RI) genes, 685 exon-skipping (SE) genes, and 131 alternatively spliced (A3SS, A5SS, and MXE) genes were differentialy expressed in the *dhx38*$^{-/-}$ embryos (Fig. 6A, Table. S3). The most significant events in differential splicing events are displayed in PSI DOWN of SE events (600/966) and PSI UP of RI events (150/966), which implies an increase in exon skipping and intron retention (Fig. 6A). Compared with the unaffected splice sites, the PSI DOWN group of SE events have significantly longer 3' and 5' introns and shorter exons. Meanwhile, the PSI UP group of RI events showed shorter introns. The PSI down group of SE events displays that the exon has lower GC content (Fig. 6C). The shorter affected exon/intron length and lower GC content may require higher accuracy for splicing factors, and therefore more sensitive to *dhx38* deletion.

The biological processes of the cell cycle, double-strand break repair, microtubule cytoskeleton, and chromosome segregation were mainly enriched among all the differentially spliced events (Fig 6B, D). They were verified by UCSC, semi-qPCR, and qRT-PCR in wild-type sibling and *dhx38* mutants (Fig 7A-B, Fig. S7). Significant splicing changes and decreased expression were observed in genes such as *mis18a*, *cenpk*, *kdm8*, *smc5*, *knl1* (chromatin segregation), *ccng2*, *ccnb2*, *aaas* (cell cycle kinase), *dtl*, *trip12*, *rad9a*, *eme1*, *tonsl*, *recql* (DNA damage), and *scrib*, *ift20*, *cep131*, *lzts2a*, *sept6a*, *mak*, *pard3ab* (microtubule cytoskeleton). Many of these genes are components of the centriole or spindle apparatus. Previous studies have shown that *cenpk, mis18a* and *knl1* mediate centromeric functions (Cheeseman et al., 2008; Medina-Pritchard et al., 2020);

The *smc5* and *kdm8* genes are involved in chromatin segregation during mitosis (Hsia et al., 2010; Wehrkamp-Richter et al., 2012); Loss of function of *ccng2* and *ccnb2* has been shown to result in a defection of chromatin condensation (Gong and Ferrell, 2010); *aaas* (also known as *aladin*) is a spatial regulator of Aurora A that plays a critical role in multiple steps of mitotic progression (Carvalhal et al., 2015); The *scrib*, *ift20*, *cep131*, *lzts2a*, *sept6a*, *mak* and *pard3ab* participate in microtubule motor activity and microtubule polymerization (Carvalho et al., 2015; Chen et al., 2009; Holdgaard et al., 2019; Hong et al., 2010; Sudo and Maru, 2008; Wang and Kung, 2012; Zhu et al., 2017). The *dtl*, *trip12*, *rad9a*, *eme1*, *tonsl*, and *recql* are essential for genome integrity and chromosomal stability (Calzetta et al., 2020; Gatti et al., 2020; Huang et al., 2019; Piwko et al., 2016; Sansam et al., 2006). Of the genes assessed, *cenpk*, *smc5*, *knl1*, *kdm8*, *eme1*, *tonsl*, *ccng2*, *ccnb2* and *aaas* are predicted to undergo premature termination codons-nonsense-mediated mRNA decay events, while *trip12*, *scrib*, *pard3b*, *sept6*, *ift20*, and *lzts2a* undergo differential isoform transition, with *mis18a*, *dtl*, *rad9a*, *mak*, and *cep131* generating disordered isoform (Fig 7C).

Given the essential role of these alternatively spliced genes in mitosis, these observations likely explain the abnormal mitosis events observed in the *dhx38* mutants. Western blot of CCNB2 in the si-DHX38-641 group also displayed decreased protein expression, compared to the si-NC or si-DHX38-325 group (Fig. 7D). All the isoform transition or NMD events of differential spliced genes are provided in Table S3-4.

Dhx38 mutants undergo p53 dependent apoptosis.

Accumulation of EMPs and HSPCs was followed by induction of apoptosis. The expression of *p53* and its target genes *p21*, *mdm2* and *puma* are up-regulated in *dhx38*^{-/-} embryos (Fig. 8A). P53 protein also appeared overtly increased in the mutants at 56 hpf (Fig. 8B). WISH assays revealed increased expression of *p53* in the CHT of the mutants at 36 hpf and in the AGM and CHT of the mutants at 56 hpf (Fig. 8C, G). We rescued the

embryos by inhibiting *p53* activity. As expected, the number of HSPCs at 56 hpf was significantly increased after incubation with the P53 inhibitor PFT-β in the *dhx38* mutants (Fig. 8D-E, H-J). Both PFT-β and *p53* mutants extended the survival ratio of the *dhx38* mutants (Fig. 8F). Taken together, these data suggest that the induction of apoptosis in *dhx38* mutant is *p53*-dependent.

Material and methods

Fish strains and embryos

Zebrafish embryos were reared and kept at 28.5 °C under standard aquaculture conditions, as described previously (Hu et al., 2019). Female and male zebrafish of the AB strain under one year of age were used. The transgenic zebrafish used in this study included Tg(*cmyb*:eGFP) (CZ273), Tg(*gata1*:dsred) (CZ64), Tg(*flk*:mCherry). Tg(*pu.1*-gal4-vp16-uas-GFP) (CZ83), Tg(*mpeg1*:eGFP) (CZ98), and were purchased from China Zebrafish Resource Center (CZRC). Tg(*mpx*:eGFP) was obtained from Prof. Zhang (Lian et al., 2018). All animal experimental procedures were reviewed and approved by the Ethics Committee of Huazhong University of Science and Technology.

Generation of *dhx38* mutants using CRISPR/Cas9 technology

Dhx38$^{-/-}$ zebrafish were generated by CRISPR/Cas9 technology as described previously (Li et al., 2021). The guide RNAs (gRNAs) were designed by CHOPCHOP (http://chopchop.cbu.uib.no/). mMESSAGE mMACHINE T7 Transcription Kit (Invitrogen) and TranscriptAid T7 High Yield Transcription Kit (Thermo Scientific) were used to generate Cas9 mRNA and gRNAs, respectively. Zebrafish carrying *dhx38* mutations were identified by Sanger sequencing.

RNA-seq

Total RNA from the trunk region of siblings and *dhx38*^{-/-} embryos at 36 hpf was extracted using Trizol (Invitrogen). With the use of Nanodrop and the Bioanalyzer 2100 (Agilent), RNA sample quality and quantity were assessed. Beijing Novogene and Biomarker used an Illumina HiSeq2000 platform to carry out RNA-Seq. RNA-Seq quality control and filtering were conducted using fastp software. Input files following quality control were aligned to the Zebrafish genome (Ensembl GRCz11) by STAR software using the 2-pass strategy. Gene expression data were extracted using featureCounts software and differential analysis was performed using edgeR (Table. S1-2). Alternative splicing analysis was implemented by the software rMATS and visualized using rmats2sashimiplot for significant differential splicing events (Table. S3-4, Fig. S7) (Li et al., 2021). Metascape (http://metascape.org) was utilized to identify GO terms enriched in the differential expression gene and differential splicing gene (Table. S1-2). RNA-seq data in this study have been uploaded to GEO under accession number GSE165203.

Whole-mount in situ hybridization

Whole-mount in situ hybridization (WISH) for zebrafish embryos was performed as described previously (Yu et al., 2019). More than 40 zebrafish embryos were used to ensure that the proportion of homozygous was above 10. The probes used for RNA in situ hybridization included *scl*, *gata1*, *pu.1*, *cmyb*, *lmo2*, *dll4*, *dab2*, *hbaeI*, *l-plastin*, *lyz*, *cebpa*, *mpeg1.1*, *mpx*, *β-eglobin*, *dhx38*, *mfap4* and *rag1*. The primers used to synthesize probes are listed in Table. S5.

Semi-qPCR and Quantitative real-time PCR (qRT-PCR)

Semi-qPCR was performed to confirm abnormal alternative splicing. Primer design for differentially spliced genes with aberrant splice sites. The PCR products were analyzed by gel electrophoresis and visualized using the Gel ultraviolet detector ZF-401. Percent

spliced in (PSI) values from 0 to 100 reflected the ratio of correct splicing from the total junction reads (Li et al., 2021). Exons/intron that are constitutively retained in all transcripts and never skipped have a PSI of 100.

qRT-PCR was conducted with AceQ qPCR SYBR Green Master Mix (Vazyme Biotech) in a StepOnePlus™ real-time PCR machine. Gene expression was normalized to GAPDH. The primers for semi-qPCR and qRT-PCR are summarized in Table. S5.

Sudan black staining

Staining solution: 0.3 g of Sudan Black (4197-25-5, sigma-aldrich) was added to 100 mL of anhydrous ethanol (64-17-5, sinopharm) and heated or ground for one to two days to dissolve completely. Buffer solution: 16 g of crystalline phenol (108-95-2, Sigma-Aldrich) dissolved in 30 mL of anhydrous ethanol was then added to 100 mL of water containing 0.3 g of sodium dihydrogen phosphate (7558-80-7, sinopharm). These solutions were stored at 4°C and used immediately after mixing the staining solution and buffer solution in a 3:2 ratio. The fixed embryos were incubated in 1 mL Sudan Black staining solution (mixed solution) for 20 min, then washed with 70% ethanol and photographed under the Nikon Eclipse 80i Advanced Research Microscope (Nikon, RRID:SCR_015572).

Neural red staining

Neutral red can be phagocytosed by macrophages and concentrated in their lysosomes, thus causing live macrophages to be labeled red. Neutral Red solution: 0.01g of Neutral Red powder was dissolved in 1mL of pure water, with completely dissolved Neutral red (10mg/mL), stored at 4 °C and protected from light. Live embryos at 36 hpf were incubated in 1 mL of neutral red staining solution (2.5 µg/mL) at 28 °C for 8h and protected from light. Embryos were washed three times in PBST for 5 minutes each, fixed with 4% PFA and photographed by ECLIPSE 80i (Nikon).

Immunofluorescence, TUNEL staining, Edu assay

Embryos were collected and fixed with 4% PFA overnight at 4 °C. After washing with PBST, embryos were soaked in acetone for 15 min. Embryos were then blocked with PBDT containing 10% goat serum at room temperature for 1 h. After blocking, embryos were incubated with the primary antibody overnight at 4 °C. The fluorescent secondary antibody was used to visualize the signals. The primary and secondary antibodies used are listed in Table. S6. The immunofluorescence signals were observed and imaged under an FV1000 confocal microscope (Olympus, RRID:SCR_020337).

TUNEL (TdT mediated dUTP Nick End Labeling) staining was performed using TUNEL BrightRed/Green Apoptosis Detection Kit (A113/A112, Vazyme); For Edu (5-Ethynyl-2'-deoxyuridine) assay, live embryos at 34 hpf were incubated in EDU (2mM) for 30min at 4 °C and then switched to freshwater for 2h. Embryos were then fixed with 4% PFA overnight at 4 °C, and apoptosis detected by the Cell-Light EdU Apollo567/488 In Vitro Kit (C10310/C10338, Ribobio). Images were taken with a Nikon Eclipse 80i Advanced Research Microscope (Nikon, RRID:SCR_015572).

Cell culture and flow analysis

The K562 cell line was obtained from Prof. Yong You's lab and tested for contamination (Zhou et al., 2021). Small interfering RNAs (siRNAs) targeting different encoding regions of human DHX38 were designed by the RiboBio company (Guangzhou, China). Two independent siRNAs were used for the Dhx38 gene to avoid off-target effects. The siDHX38-641 RNA is at the c.641 position of the human DHX38 gene, and siDHX38-328 is at c.328. A nonspecific siRNA duplex was used as an siRNA negative control (si-NC). The silencing effects of these two siRNAs were confirmed by western blot. The sequences of the siRNAs used in this study are listed in Table. S7. After 72 h of transfection with DHX38 siRNA in 12-well plates according to the protocol, suspension cells were then collected and washed with cold PBS. Cells were then resuspended in 700

µL of PBS with 300 µL of 70% ice-cold ethanol slowly added on a gentle shaker. Cells were then fixed overnight in the freezer at -20 °C. After washing the cells with PBS, 1 ml of PI staining (Final conc. PI, 20 µg/ml; Triton X100, 0.1%; RNase A, 0.2 mg/ml) solution was added, the cells were evenly dispersed and stained for at least 30 min protected from light. Analysis was performed on Cytoflex S (Beckman, RRID:SCR_019627) and cell cycle calculations were performed with flowjo software using the Dean-Jett-Fox model (RRID:SCR_008520).

Statistical analysis

For statistical analysis, data represent as mean ± SD, and a statistically significant difference between control and experimental groups was determined by an unpaired, two-tailed Student's t-test. The level of significance was set to $P < 0.05$.

Discussion

In this study, our findings demonstrate that Dhx38 is essential for the maintenance and differentiation of EMPs and HSPCs during zebrafish embryogenesis. The importance of EMPs in fetal hematopoiesis has not been fully elucidated to date. Herein, we emphasize the key role of the splicing factor Dhx38 in EMP development. In *dhx38*$^{-/-}$ zebrafish, EMPs accumulated, but failed to differentiate into mature myeloid cells. This result suggests that loss of *dhx38* may lead to fetal hematopoiesis defects, which may prevent the embryo from surviving. Moreover, EMPs give rise to macrophage precursors that distribute within embryonic tissues and differentiate into adult tissue-resident macrophage subsets, such as the lkupffer cells in the liver, langerhan cells in the epidermis, andalveolar macrophages in the lungs. Impaired EMP differentiation caused by *dhx38* deletion may result in the loss of the tissue-resident macrophage pool in adults, leading to related diseases.

Previously, we demonstrated that the splicing factor Bcas2, is vital for HSPC maintenance by regulating p53 signaling to inhibit apoptosis (Yu et al., 2019). Here we report that the deletion of splicing factor Dhx38 inhibits cell cycle progression and differentiation of EMPs and HSPCs, and increases apoptosis in a p53-dependent-manner. These defective phenotypes observed in EMPs overlapped with that of HSPCs, pointing to common mechanisms underlying their development and maintenance.

Since both EMPs and HSPCs exhibit hematopoietic progenitor cell characteristics, they are likely to have similar pathogenic mechanisms yet dinstinct regulatory preferences. Of note, EMPs with fetal characteristics are developmentally restricted, but can be used for long-term multilineage reconstitution upon transplantation into adult recipients (Chen et al., 2011). This hematological model can serve as a useful model for understanding the temporal and spatial control of EMP and HSPC and the etiology of hematopoietic malignancies, and facilitating the development and testing of novel therapeutic interventions.

Splicing factors may be directly related to the regulation of mitosis or could result from the indirect consequence of compromised splicing. Previous studies have revealed that mutation in DHX38 affects the function of Aurora B and centromeric heterochromatin, which results in defective chromosome segregation in the mitotic phase (Nishimura et al., 2019; Vijayakumari et al., 2019). However, only a limited number of genes have been characterized as the targets of Dhx38 in these studies. Our study is the first to elucidate the role of the splicing factor Dhx38 in regulating mitosis and differentiation by alternative splicing during hematopoiesis. As RNA splicing is often tissue-specific, it is plausible that the Dhx38-regulated program in EMPs and HSPCs differs from that of other tissues. Here, we found that deletion of *dhx38* causes mitosis arrest in EMPs and HSPCs, accompanied by a 'grape' karyotype due to the defects in chromosome alignment. RNA-seq analysis identified abnormal splicing genes regulated by Dhx38, which related to chromosome segregation, microtubule cytoskeleton, cell cycle kinase, and DNA damage (Fig. 6C, D). Although molecular mechanisms of how each process affects the mitosis of

EMPs and HSPCs are currently unknown, it is likely that multiple regulatory mechanisms of DHX38 co-exist in cells and work together to regulate the cell cycle.

In addition to regulating mitosis, deletion of *dhx38* leads to reduced S-phase and increased DNA damage in EMPs and HSPCs, implying an important role for Dhx38 in the maintenance of genomic integrity during DNA replication. Splicing factor depletion could affect DNA replication during S phase, resulting in R-loop formation and associated genomic instability, which activates the DNA damage response (Chakraborty et al., 2018). Mitotic mistakes, such as lagging chromosomes, and mitotic delay can also cause DNA damage, which can trigger p53-dependent apoptosis (Edwards et al., 2021; Ganem and Pellman, 2012; Hayashi and Karlseder, 2013; Jelluma and Kops, 2014). A defective DNA damage response can lead to genomic instability underlying many diseases, including hematological disorders and cancer (Bugai et al., 2019; Yoshioka et al., 2021). Since the interplay between cell cycle inhibition, DNA damage, and apoptosis is complex, and how these processes affect each other in *dhx38* mutants are unknown, further investigation is required.

In summary, the most striking result to emerge from the data is the new insight into the role of Dhx38 in maintaining differentiation and survival of EMPs and HSPCs, by regulating pre-mRNA splicing of genes involved in mitosis. We hypothesize that mutation of splicing factors in cells with high proliferative requirements, including hematopoietic progenitors, neural progenitors or retinal progenitors, may share similar phenotypes. Mutations of splicing factors in AML and related myeloid malignancies have been confirmed, thus, the study contributes to our understanding of the potential role of altered pre-mRNA splicing in the pathogenesis of clonal hematopoietic malignancies.

paper, Dr. Yong You, Huazhong University of Science and Technology, for providing K562 cells.

Data availability

RNA-seq: GSE165203: https://www.ncbi.nlm.nih.gov/geo/query/acc.cgi?acc=GSE165203

UCSC track: https://genome.ucsc.edu/s/yjzhang2013/danRer11

The raw data underlying graphs and charts, including uncropped versions of gels and western blots, has been deposited in Mendeley:

https://data.mendeley.com/datasets/tvfv9h569b/draft?a=1bfa3c21-d0f8-48aa-ba4b-b68d18cf8ccb

The *dhx38* knockout zebrafish lines generated in this study have been deposited within the China Zebrafish Resource Center (CZRC).

This study did not generate any new/unique reagents. All stable reagents generated in this study are available from the corresponding authors upon reasonable request.

References

Baeten, J. T. and de Jong, J. L. O. (2018). Genetic Models of Leukemia in Zebrafish. *Front Cell Dev Biol* **6**, 115.

Baralle, F. E. and Giudice, J. (2017). Alternative splicing as a regulator of development and tissue identity. *Nat Rev Mol Cell Bio* **18**, 437-451.

Bertrand, J. Y., Cisson, J. L., Stachura, D. L. and Traver, D. (2010). Notch signaling distinguishes 2 waves of definitive hematopoiesis in the zebrafish embryo. *Blood* **115**, 2777-2783.

Bertrand, J. Y., Kim, A. D., Teng, S. and Traver, D. (2008). CD41+ cmyb+ precursors colonize the zebrafish pronephros by a novel migration route to initiate adult hematopoiesis. *Development* **135**, 1853-1862.

Bertrand, J. Y., Kim, A. D., Violette, E. P., Stachura, D. L., Cisson, J. L. and Traver, D. (2007). Definitive hematopoiesis initiates through a committed erythromyeloid progenitor in the zebrafish embryo. *Development* **134**, 4147-4156.

Bugai, A., Quaresma, A. J. C., Friedel, C. C., Lenasi, T., Duster, R., Sibley, C. R., Fujinaga, K., Kukanja, P., Hennig, T., Blasius, M., et al. (2019). P-TEFb Activation by RBM7 Shapes a Pro-survival Transcriptional Response to Genotoxic Stress. *Mol Cell* **74**, 254-267 e210.

Calzetta, N. L., Gonzalez Besteiro, M. A. and Gottifredi, V. (2020). Mus81-Eme1-dependent aberrant processing of DNA replication intermediates in mitosis impairs genome integrity. *Sci Adv* **6**.

Carvalhal, S., Ribeiro, S. A., Arocena, M., Kasciukovic, T., Temme, A., Koehler, K., Huebner, A. and Griffis, E. R. (2015). The nucleoporin ALADIN regulates Aurora A localization to ensure robust mitotic spindle formation. *Mol Biol Cell* **26**, 3424-3438.

Carvalho, C. A., Moreira, S., Ventura, G., Sunkel, C. E. and Morais-de-Sa, E. (2015). Aurora A Triggers Lgl Cortical Release during Symmetric Division to Control Planar Spindle Orientation. *Curr Biol* **25**, 53-60.

Chakraborty, P., Huang, J. T. J. and Hiom, K. (2018). DHX9 helicase promotes R-loop formation in cells with impaired RNA splicing. *Nat Commun* **9**, 4346.

Cheeseman, I. M., Hori, T., Fukagawa, T. and Desai, A. (2008). KNL1 and the CENP-H/I/K complex coordinately direct kinetochore assembly in vertebrates. *Mol Biol Cell* **19**, 587-594.

Chen, L., Kostadima, M., Martens, J. H. A., Canu, G., Garcia, S. P., Turro, E., Downes, K., Macaulay, I. C., Bielczyk-Maczynska, E., Coe, S., et al. (2014). Transcriptional diversity during lineage commitment of human blood progenitors. *Science* **345**, 1251033.

Chen, M. J., Li, Y., De Obaldia, M. E., Yang, Q., Yzaguirre, A. D., Yamada-Inagawa, T., Vink, C. S., Bhandoola, A., Dzierzak, E. and Speck, N. A. (2011). Erythroid/myeloid progenitors and hematopoietic stem cells originate from distinct populations of endothelial cells. *Cell Stem Cell* **9**, 541-552.

Chen, T. C., Lee, S. A., Chan, C. H., Juang, Y. L., Hong, Y. R., Huang, Y. H., Lai, J. M., Kao, C. Y. and Huang, C. Y. F. (2009). Cliques in mitotic spindle network bring kinetochore-associated complexes to form dependence pathway. *Proteomics* **9**, 4048-4062.

Da'as, S. I., Coombs, A. J., Balci, T. B., Grondin, C. A., Ferrando, A. A. and Berman, J. N. (2012). The zebrafish reveals dependence of the mast cell lineage on Notch signaling in vivo. *Blood* **119**, 3585-3594.

Dai, Y. M., Zhu, L., Huang, Z. B., Zhou, M. Y., Jin, W., Liu, W., Xu, M. C., Yu, T., Zhang, Y. Y., Wen, Z. L., et al. (2016). Cebp alpha is essential for the embryonic myeloid progenitor and neutrophil maintenance in zebrafish. *Journal of Genetics and Genomics* **43**, 593-600.

Danilova, N., Kumagai, A. and Lin, J. (2010). p53 upregulation is a frequent response to deficiency of cell-essential genes. *PLoS One* **5**, e15938.

De La Garza, A., Cameron, R. C., Nik, S., Payne, S. G. and Bowman, T. V. (2016). Spliceosomal component Sf3b1 is essential for hematopoietic differentiation in zebrafish. *Exp Hematol* **44**, 826-837 e824.

Dege, C., Fegan, K. H., Creamer, J. P., Berrien-Elliott, M. M., Luff, S. A., Kim, D., Wagner, J. A., Kingsley, P. D., McGrath, K. E., Fehniger, T. A., et al. (2020). Potently Cytotoxic Natural Killer Cells Initially Emerge from Erythro-Myeloid Progenitors during Mammalian Development. *Dev Cell* **53**, 229-239 e227.

Edwards, D. M., Mitchell, D. K., Abdul-Sater, Z., Chan, K. K., Sun, Z., Sheth, A., He, Y., Jiang, L., Yuan, J., Sharma, R., et al. (2021). Mitotic Errors Promote Genomic Instability and Leukemia in a Novel Mouse Model of Fanconi Anemia. *Front Oncol* **11**, 752933.

Fica, S. M., Oubridge, C., Galej, W. P., Wilkinson, M. E., Bai, X. C., Newman, A. J. and Nagai, K. (2017). Structure of a spliceosome remodelled for exon ligation. *Nature* **542**, 377-380.

Forrester, A. M., Berman, J. N. and Payne, E. M. (2012). Myelopoiesis and myeloid leukaemogenesis in the zebrafish. *Adv Hematol* **2012**, 358518.

Frame, J. M., Fegan, K. H., Conway, S. J., McGrath, K. E. and Palis, J. (2016). Definitive Hematopoiesis in the Yolk Sac Emerges from Wnt-Responsive Hemogenic Endothelium Independently of Circulation and Arterial Identity. *Stem Cells* **34**, 431-444.

Ganem, N. J. and Pellman, D. (2012). Linking abnormal mitosis to the acquisition of DNA damage. *J Cell Biol* **199**, 871-881.

Gatti, M., Imhof, R., Huang, Q., Baudis, M. and Altmeyer, M. (2020). The Ubiquitin Ligase TRIP12 Limits PARP1 Trapping and Constrains PARP Inhibitor Efficiency. *Cell Rep* **32**, 107985.

Gong, D. and Ferrell, J. E. (2010). The Roles of Cyclin A2, B1, and B2 in Early and Late Mitotic Events. *Molecular Biology of the Cell* **21**, 3149-3161.

Gottgens, B., Broccardo, C., Sanchez, M. J., Deveaux, S., Murphy, G., Gothert, J. R., Kotsopoulou, E., Kinston, S., Delaney, L., Piltz, S., et al. (2004). The scl +18/19 stem cell enhancer is not required for hematopoiesis: identification of a 5' bifunctional hematopoietic-endothelial enhancer bound by Fli-1 and Elf-1. *Mol Cell Biol* **24**, 1870-1883.

Han, S., Park, J. and Lee, D. H. (2015). Protein DHX38 is a novel inhibitor of protein phosphatase 4. *Animal Cells and Systems* **19**, 236-244.

Hayashi, M. T. and Karlseder, J. (2013). DNA damage associated with mitosis and cytokinesis failure. *Oncogene* **32**, 4593-4601.

Hoeffel, G., Chen, J., Lavin, Y., Low, D., Almeida, F. F., See, P., Beaudin, A. E., Lum, J., Low, I., Forsberg, E. C., et al. (2015). C-Myb(+) erythro-myeloid progenitor-derived fetal monocytes give rise to adult tissue-resident macrophages. *Immunity* **42**, 665-678.

Holdgaard, S. G., Cianfanelli, V., Pupo, E., Lambrughi, M., Lubas, M., Nielsen, J. C., Eibes, S., Maiani, E., Harder, L. M., Wesch, N., et al. (2019). Selective autophagy maintains centrosome integrity and accurate mitosis by turnover of centriolar satellites. *Nat Commun* **10**, 4176.

Hong, E., Jayachandran, P. and Brewster, R. (2010). The polarity protein Pard3 is required for centrosome positioning during neurulation. *Dev Biol* **341**, 335-345.

Hsia, D. A., Tepper, C. G., Pochampalli, M. R., Hsia, E. Y., Izumiya, C., Huerta, S. B., Wright, M. E., Chen, H. W., Kung, H. J. and Izumiya, Y. (2010). KDM8, a H3K36me2 histone demethylase that acts in the cyclin A1 coding region to regulate cancer cell proliferation. *Proc Natl Acad Sci U S A* **107**, 9671-9676.

Hu, X., Lu, Z., Yu, S., Reilly, J., Liu, F., Jia, D., Qin, Y., Han, S., Liu, X., Qu, Z., et al. (2019). CERKL regulates autophagy via the NAD-dependent deacetylase SIRT1. *Autophagy* **15**, 453-465.

Huang, L., Meng, T. G., Ma, X. S., Wang, Z. B., Qi, S. T., Chen, Q., Zhang, Q. H., Liang, Q. X., Wang, Z. W., Hu, M. W., et al. (2019). Rad9a is involved in chromatin decondensation and post-zygotic embryo development in mice. *Cell Death Differ* **26**, 969-980.

Jelluma, N. and Kops, G. J. (2014). Collateral genome instability by DNA damage in mitosis. *Cancer Discov* **4**, 1256-1258.

Latif, Z., Chakchouk, I., Schrauwen, I., Lee, K., Santos-Cortez, R. L. P., Abbe, I., Acharya, A., Jarral, A., Ali, I., Ullah, E., et al. (2018). Confirmation of the Role of DHX38 in the Etiology of Early-Onset Retinitis Pigmentosa. *Invest Ophth Vis Sci* **59**, 4552-4557.

Li, D., Xue, W., Li, M., Dong, M., Wang, J., Wang, X., Li, X., Chen, K., Zhang, W., Wu, S., et al. (2018a). VCAM-1(+) macrophages guide the homing of HSPCs to a vascular niche. *Nature* **564**, 119-124.

Li, J., Liu, F., Lv, Y., Sun, K., Zhao, Y., Reilly, J., Zhang, Y., Tu, J., Yu, S., Liu, X., et al. (2021). Prpf31 is essential for the survival and differentiation of retinal progenitor cells by modulating alternative splicing. *Nucleic Acids Res* **49**, 2027-2043.

Li, Z., Liu, S., Xu, J., Zhang, X., Han, D., Liu, J., Xia, M., Yi, L., Shen, Q., Xu, S., et al. (2018b). Adult Connective Tissue-Resident Mast Cells Originate from Late Erythro-Myeloid Progenitors. *Immunity* **49**, 640-653 e645.

Lian, J. W., Chen, J. K., Wang, K., Zhao, L. F., Meng, P., Yang, L. T., Wei, J. Y., Ma, N., Xu, J., Zhang, W. Q., et al. (2018). Alas1 is essential for neutrophil maturation in zebrafish. *Haematologica* **103**, 1785-1795.

Ma, Y., Barnett, T., Chai, L., Yang, J. C., Alipio, Z., Pei, L., Amin, H. M., Fink, L., Di, C. H. and Yan, H. (2006). DEAH-box splicing factor gene, prp16 amplification in acute myeloid leukemia. *Blood* **108**, 198b-198b.

Mass, E., Jacome-Galarza, C. E., Blank, T., Lazarov, T., Durham, B. H., Ozkaya, N., Pastore, A., Schwabenland, M., Chung, Y. R., Rosenblum, M. K., et al. (2017). A somatic mutation in erythro-myeloid progenitors causes neurodegenerative disease. *Nature* **549**, 389-393.

McGrath, K. E., Frame, J. M., Fromm, G. J., Koniski, A. D., Kingsley, P. D., Little, J., Bulger, M. and Palis, J. (2011). A transient definitive erythroid lineage with unique regulation of the beta-globin locus in the mammalian embryo. *Blood* **117**, 4600-4608.

Medina-Pritchard, B., Lazou, V., Zou, J., Byron, O., Abad, M. A., Rappsilber, J., Heun, P. and Jeyaprakash, A. A. (2020). Structural basis for centromere maintenance by Drosophila CENP-A chaperone CAL1. *EMBO J* **39**, e103234.

Mitroulis, I., Ruppova, K., Wang, B., Chen, L. S., Grzybek, M., Grinenko, T., Eugster, A., Troullinaki, M., Palladini, A., Kourtzelis, I., et al. (2018). Modulation of Myelopoiesis Progenitors Is an Integral Component of Trained Immunity. *Cell* **172**, 147-161 e112.

Nishimura, K., Cho, Y., Tokunaga, K., Nakao, M., Tani, T. and Ideue, T. (2019). DEAH box RNA helicase DHX38 associates with satellite I noncoding RNA involved in chromosome segregation. *Genes Cells* **24**, 585-590.

Pellagatti, A. and Boultwood, J. (2020). Splicing factor mutant myelodysplastic syndromes: Recent advances. *Adv Biol Regul* **75**, 100655.

Piwko, W., Mlejnkova, L. J., Mutreja, K., Ranjha, L., Stafa, D., Smirnov, A., Brodersen, M. M., Zellweger, R., Sturzenegger, A., Janscak, P., et al. (2016). The MMS22L-TONSL heterodimer directly promotes RAD51-dependent recombination upon replication stress. *EMBO J* **35**, 2584-2601.

Sansam, C. L., Shepard, J. L., Lai, K., Ianari, A., Danielian, P. S., Amsterdam, A., Hopkins, N. and Lees, J. A. (2006). DTL/CDT2 is essential for both CDT1 regulation and the early G2/M checkpoint. *Genes Dev* **20**, 3117-3129.

Sudo, H. and Maru, Y. (2008). LAPSER1/LZTS2: a pluripotent tumor suppressor linked to the inhibition of katanin-mediated microtubule severing. *Human Molecular Genetics* **17**, 2524-2540.

Vijayakumari, D., Sharma, A. K., Bawa, P. S., Kumar, R., Srinivasan, S. and Vijayraghavan, U. (2019). Early splicing functions of fission yeast Prp16 and its unexpected requirement for gene Silencing is governed by intronic features. *Rna Biol* **16**, 754-769.

Wang, L. Y. and Kung, H. J. (2012). Male germ cell-associated kinase is overexpressed in prostate cancer cells and causes mitotic defects via deregulation of APC/C-CDH1. *Oncogene* **31**, 2907-2918.

Wehrkamp-Richter, S., Hyppa, R. W., Prudden, J., Smith, G. R. and Boddy, M. N. (2012). Meiotic DNA joint molecule resolution depends on Nse5-Nse6 of the Smc5-Smc6 holocomplex. *Nucleic Acids Res* **40**, 9633-9646.

Weinreb, J. T., Ghazale, N., Pradhan, K., Gupta, V., Potts, K. S., Tricomi, B., Daniels, N. J., Padgett, R. A., De Oliveira, S., Verma, A., et al. (2021). Excessive R-loops trigger an inflammatory cascade leading to increased HSPC production. *Dev Cell* **56**, 627-640 e625.

Xia, J., Kang, Z., Xue, Y., Ding, Y., Gao, S., Zhang, Y., Lv, P., Wang, X., Ma, D., Wang, L., et al. (2021). A single-cell resolution developmental atlas of hematopoietic stem and progenitor cell expansion in zebrafish. *Proc Natl Acad Sci U S A* **118**.

Yokomizo, T., Mori, S., Kurokawa, M., Osato, M. and Komatsu, N. (2018). Hlf expression marks the developmental pathway for hematopoietic stem cells but not for erythroid-myeloid progenitors. *Cancer Sci* **109**, 1093-1093.

Yoshioka, K. I., Kusumoto-Matsuo, R., Matsuno, Y. and Ishiai, M. (2021). Genomic Instability and Cancer Risk Associated with Erroneous DNA Repair. *Int J Mol Sci* **22**.

Yu, S., Jiang, T., Jia, D., Han, Y., Liu, F., Huang, Y., Qu, Z., Zhao, Y., Tu, J., Lv, Y., et al. (2019). BCAS2 is essential for hematopoietic stem and progenitor cell maintenance during zebrafish embryogenesis. *Blood* **133**, 805-815.

Zhou, S., Li, W., Xiao, Y., Zhu, X., Zhong, Z., Li, Q., Cheng, F., Zou, P., You, Y. and Zhu, X. (2021). A novel chimeric antigen receptor redirecting T-cell specificity towards CD26(+) cancer cells. *Leukemia* **35**, 119-129.

Zhu, X., Liang, Y. W., Gao, F. and Pan, J. M. (2017). IFT54 regulates IFT20 stability but is not essential for tubulin transport during ciliogenesis. *Cell Mol Life Sci* **74**, 3425-3437.
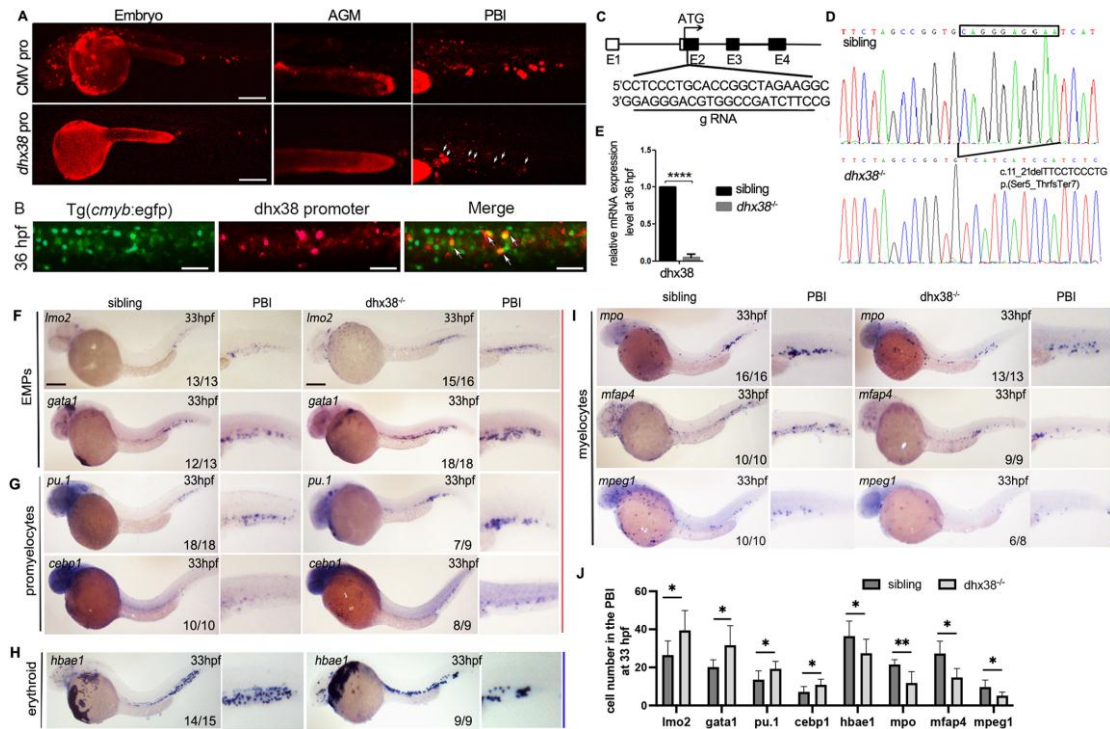
Figures

Fig. 1 Knockout of *dhx38* in zebrafish impaired EMP differentiation.

A In vivo imaging expression of CMV promoter vector and *dhx38* promoter vector in wildtype embryos. Scale bars, 200 μm. *Dhx38* promotor mainly drives mCherry expression in the PBI region. **B** Phenotype distribution plot of *dhx38* expression in Tg(*cmyb*:eGFP) at 36 hpf. White arrowheads indicate the co-expression of *dhx38* and *cmyb*. Scale bars, 50 μm. **C** A schematic diagram of the *dhx38* gRNA locus. **D** DNA sequencing identified a 10 bp deletion of cDNA (c.11_21delTTCCTCCCTG), which predicts a truncated protein (p.Ser5_ThrfsTer7). **E** qRT-PCR shows a significant decrease of *dhx38* mRNA in the *dhx38* mutants. **F, G** WISH results show expression of the EMP marker *lmo2/gata1* and promyelocytes marker *pu.1* and *cebp1* in the *dhx38*^{-/-} embryo are increased in the *dhx38* mutant at 33 hpf. Red line denotes increased expression. Scale bar, 200 μm. **H, I** WISH results reflecting the expression of mature myelocytes (*mpx*, *mfap4*, *mpeg1*) and erythrocytes (*hbae1*), are decreased in the *dhx38*

mutant at 33 hpf. Blue line denotes decreased expression. Scale bar, 200 μm. **J** Quantification of cells from (F-I), respectively; two-tailed Student's t-test; *p < 0.05, **p < 0.01; error bars, mean ± SD.
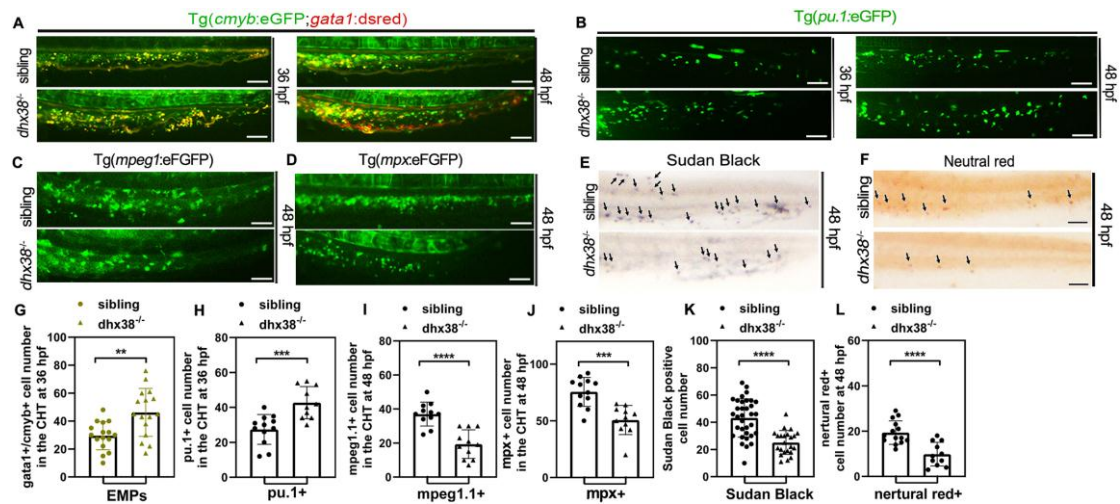
Fig. 2 Maturation of erythro-myeloid cells are perturbed in the *dhx38* mutants.

A In vivo imaging of *gata1*⁺*cmyb*⁺ (EMPs) in the PBI region of Tg(*cmyb*:eGFP;gata1:dsred) fish. At 36 hpf and 48 hpf, the number of EMPs (yellow fluorescence) in the *dhx38*⁻/⁻ zebrafish are both higher as compared to wild-type siblings. Scale bars, 50 μm. sibling, n=16; *dhx38*⁻/⁻, n=16; performed with three replicates, **p=0.002. **B** In vivo imaging of Tg(*pu.1*:eGFP) fish reflects that promyelocytes are increased in the PBI region of *dhx38* mutants at 36 hpf and 48 hpf. Scale bars, 50 μm. sibling, n=12; *dhx38*⁻/⁻, n=10; performed with three replicates, ***p=0.0006. **C** In vivo imaging of macrophages in Tg(*mpeg1*:eGFP) also shows a decreased branched cell number in the *dhx38* mutant at 48 hpf. Scale bars, 50 μm. sibling, n=11; *dhx38*⁻/⁻, n=11; performed with three replicates, ****p=0.00003. **D** In vivo imaging of granulocyte in Tg(*mpx*:eGFP) displays a decreased number in the *dhx38* mutant at 48 hpf. Scale bars, 50 μm. sibling, n=12; *dhx38*⁻/⁻, n=11; performed with three replicates, ***p=0.00013. **E** Sudan Black staining in *dhx38*⁻/⁻ zebrafish shows that mature granulocytes are decreased at 48 hpf. White arrows indicate granulocytes. Scale bars, 50 μm. sibling, n=34; *dhx38*⁻/⁻, n=23; performed with three replicates, ****p=0.000001. **F** Neutral red staining shows significantly decreased numbers of functional macrophages. Black arrows indicate macrophages. Scale bars, 50 μm. sibling, n=14; *dhx38*⁻/⁻, n=11; performed with three replicates, ***p=0.00014. **G-L** Quantification of cells from (A-G), respectively; two-tailed Student's t-test; *p < 0.05, **p < 0.01, ***p < 0.001, ****p < 0.0001; error bars, mean ± SD.
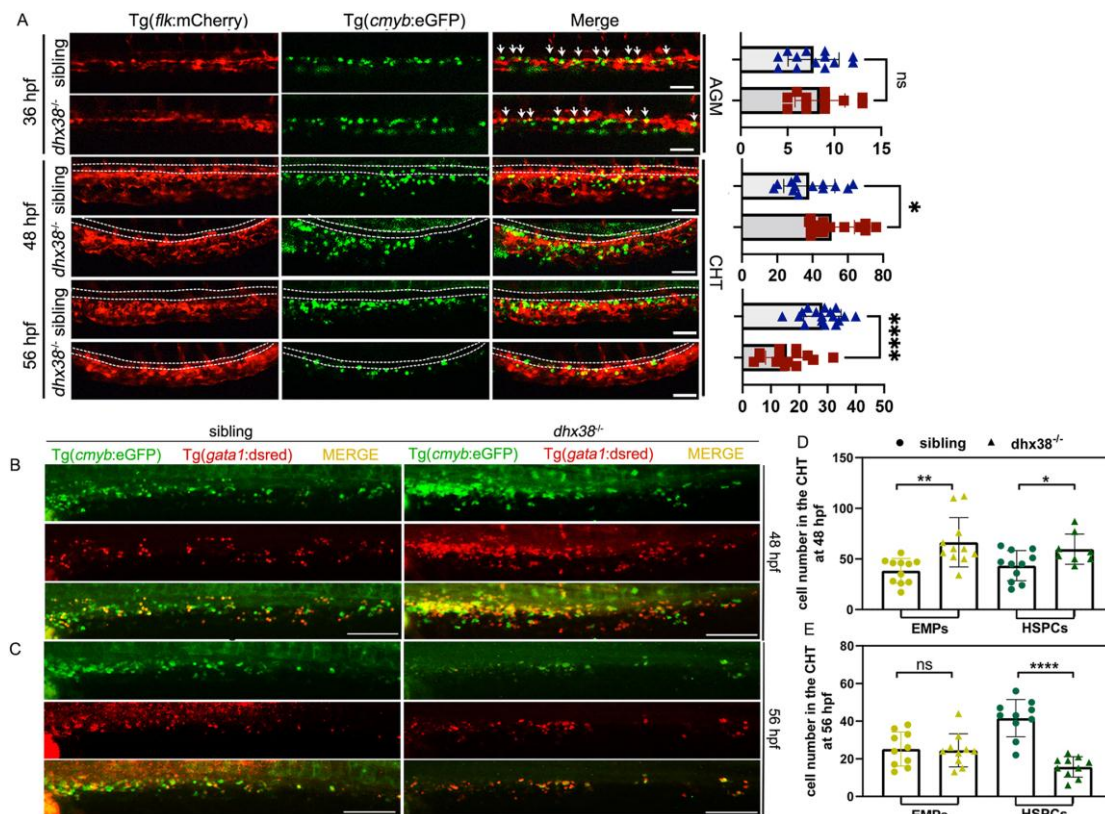
Fig. 3 Loss of *dhx38* impairs definitive hematopoiesis.

A In vivo imaging of hematopoietic progenitor cells in Tg(*cmyb*:eGFP;*flk*:mCherry) at 36hpf, 48 hpf and 56 hpf. The double-positive fluorescence (white arrowheads) in the VDA region shows that hemogenic endothelium emerges normally in the *dhx38* mutants. sibling, n=13; *dhx38$^{-/-}$*, n=13; two-tailed Student's t test; p=0.51, not significant. However, the number of *cmyb$^+$* cells in the *dhx38* mutants are increased at 48 hpf, but decreased at 56 hpf. 48 hpf sibling, n=14; 48 hpf *dhx38$^{-/-}$*, n=19; two-tailed Student's t test; *p=0.016; 56hpf sibling, n=19; 56 hpf *dhx38$^{-/-}$*, n=15; two-tailed Student's t test; ****p=0.000023. The white dotted line represents the caudal artery (CA). Scale bars, 200 μm. Quantification of cells from 36 hpf, 48 hpf, and 56hpf, respectively; two-tailed Student's t-test; *p < 0.05, **p < 0.01, ***p < 0.001, ****p < 0.0001; error bars, mean ± SD. **B** Immunostaining of Tg(*cmyb*:eGFP;*gata1*:dsred) fish at 48 hpf shows an increase in the number of *cmyb$^+$gata1$^+$* (EMPs) and *cmyb$^+$gata1$^-$* (HSPCs) in the CHT of *dhx38* mutants. Scale bars, 200 um. **C** The statistics of *cmyb$^+$gata1$^+$* and *cmyb$^+$gata1$^-$* cell numbers from

(B). sibling, n=11; *dhx38*$^{-/-}$, n=11; two-tailed Student's t test; EMPs **p=0.0026; HSPCs *p=0.031. **D** Immunostaining of Tg(*cmyb*:eGFP;*gata1*:dsred) fish at 56 hpf demonstartes a decreased number of *cmyb*$^{+}$*gata1*$^{+}$ EMPs and *cmyb*$^{+}$*gata1*$^{-}$ HSPCs in the CHT of *dhx38* mutants. Scale bars, 200 μm. **E** The statistics of *cmyb*$^{+}$*gata1*$^{+}$ and *cmyb*$^{+}$*gata1*$^{-}$ number from (e). sibling, n=10; *dhx38*$^{-/-}$, n=10; two-tailed Student's t test; EMPs p=0.86; HSPCs ****p= 0.0000009.
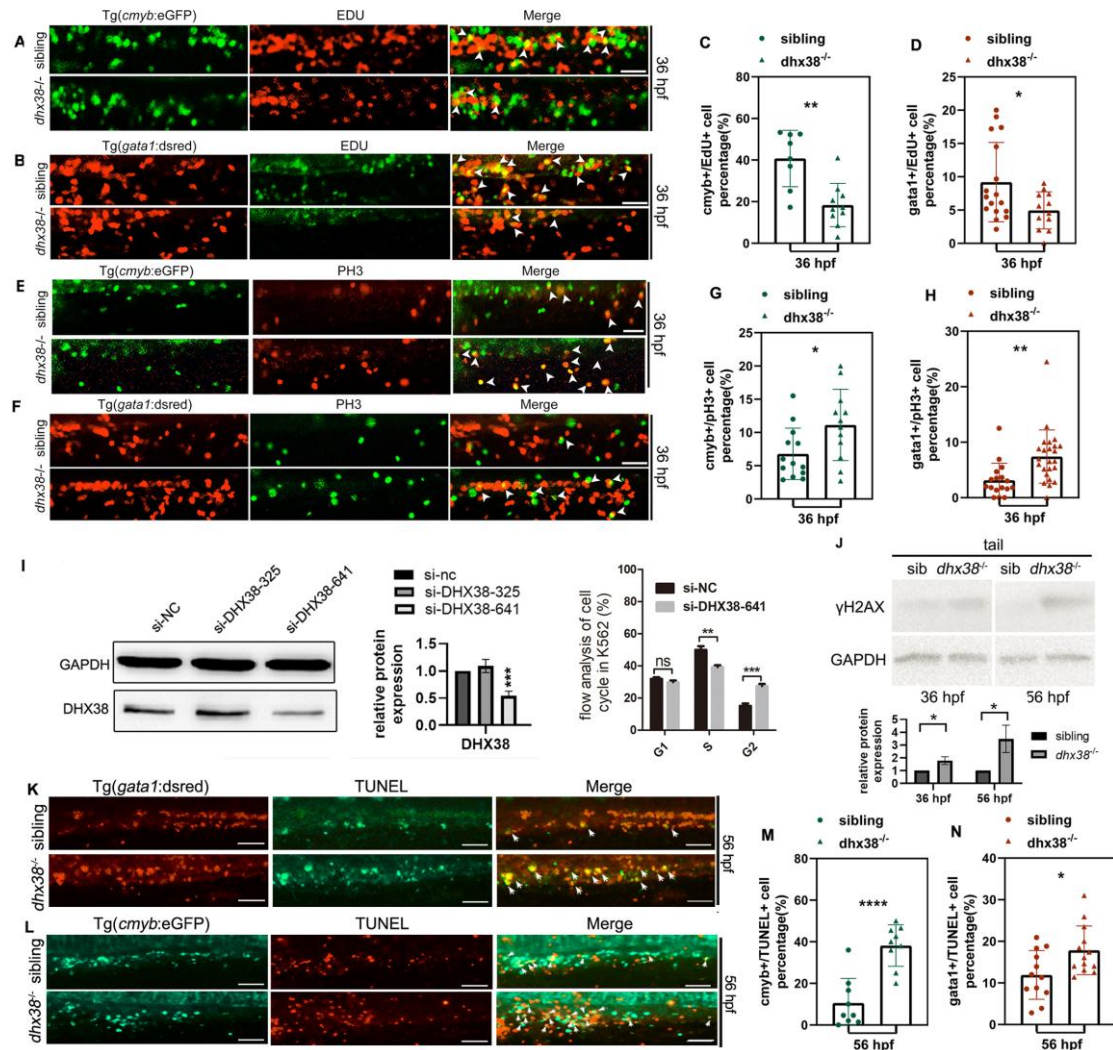
Fig. 4 Dhx38 deficiency induces abnormal mitosis and apoptosis of EMPs and HSPCs in zebrafish.

A EdU assay in Tg(*gata1*:dsred) indicates an increase of *gata1*⁺ cells in the S phase in *dhx38*⁻/⁻ embryos at 36 hpf. White arrows indicate the co-localization of *gata1* and EdU. Scale bars, 50 μm. sibling, n=17; *dhx38*⁻/⁻, n=12; performed with three replicates; *p=0.029. **B** EdU assay in Tg(*cmyb*:eGFP) indicates an increase of *cmyb*⁺ cells in the S phase of *dhx38*⁻/⁻ embryos at 36 hpf. White arrows indicate the co-localization of *cmyb* and EdU. Scale bars, 50 μm. sibling, n=8; *dhx38*⁻/⁻, n=10; performed with three replicates; **p=0.001. **C, D** The statistics of double-positive fluorescence number from (A-B), respectively. two-tailed Student's t-test; *p < 0.05, **p < 0.01, ***p < 0.001, ****p < 0.0001;

error bars, mean ± SD. **E** Double immunostaining of Tg(*gata1*:dsred) and pH3 shows that *gata1*⁺ cells in the M phase are elevated in the *dhx38* mutants at 36 hpf. White arrow indicates the co-localization of *gata1* and pH3. Scale bars, 50 μm. sibling, n=17; *dhx38*⁻ᐟ⁻, n=24; performed with three replicates; **p=0.0025. **F** Double immunostaining of Tg(*cmyb*:eGFP) and pH3 shows that *cmyb*⁺ cells in the M phase are also elevated in the *dhx38* mutants at 36 hpf. White arrow indicates the co-localization of *cmyb* and pH3. Scale bars, 50 μm. sibling, n=13; *dhx38*⁻ᐟ⁻, n=12; performed with three replicates; *p=0.028. **G, H** The statistics of double-positive fluorescence number from (E-F), respectively. two-tailed Student's t-test; *$p < 0.05$, **$p < 0.01$, ***$p < 0.001$,****$p < 0.0001$; error bars, mean ± SD. **I** The siDHX38-641 siRNA is at the c.641 position of the human DHX38 gene, siDHX38-328 is at c.328. The silencing effects of these two siRNAs were confirmed by western blot. Western of DHX38 shows efficiency of DHX38 knockdown in the si-DHX38-641 group, but not the si-DHX38-325 group. Flow analysis cell cycle after treatment with si-DHX38-641, showing a decrease of cells in the S phase and an increase of cells in the M phase. performed with six replicates; two-tailed Student's t-test, ns p=0.18, **p=0.001, ***p=0.0001. **J** The protein levels of γH2AX in siblings and *dhx38*⁻ᐟ⁻ zebrafish at 36 and 56 hpf were detected by western blot. GAPDH was used to normalize protein loading. n=3, 36 hpf *p=0.01, 48 hpf *p=0.015. **K, L** TUNEL experiment in Tg(*cmyb*:eGFP) and Tg(*gata1*:dsred) shows that apoptotic *cmyb*⁺ and *gata1*⁺ cells are increased in the *dhx38* mutants at 56 hpf. The double-positive fluorescence demonstrates that *cmyb*⁺ and *gata1*⁺ cells are undergo apoptosis. Scale bars, 50 μm. *gata1*⁺ sibling, n=12; *gata1*⁺ *dhx38*⁻ᐟ⁻, n=13; performed with three replicates; *p=0.019; *cmyb*⁺ sibling, n=9; *gata1*⁺ *dhx38*⁻ᐟ⁻, n=9; performed with three replicates; ****p=0.00006. **M, N** The statistics of double-positive fluorescence number from (K-L), respectively. two-tailed Student's t-test; *$p < 0.05$, **$p < 0.01$, ***$p < 0.001$, ****$p < 0.0001$; error bars, mean ± SD.
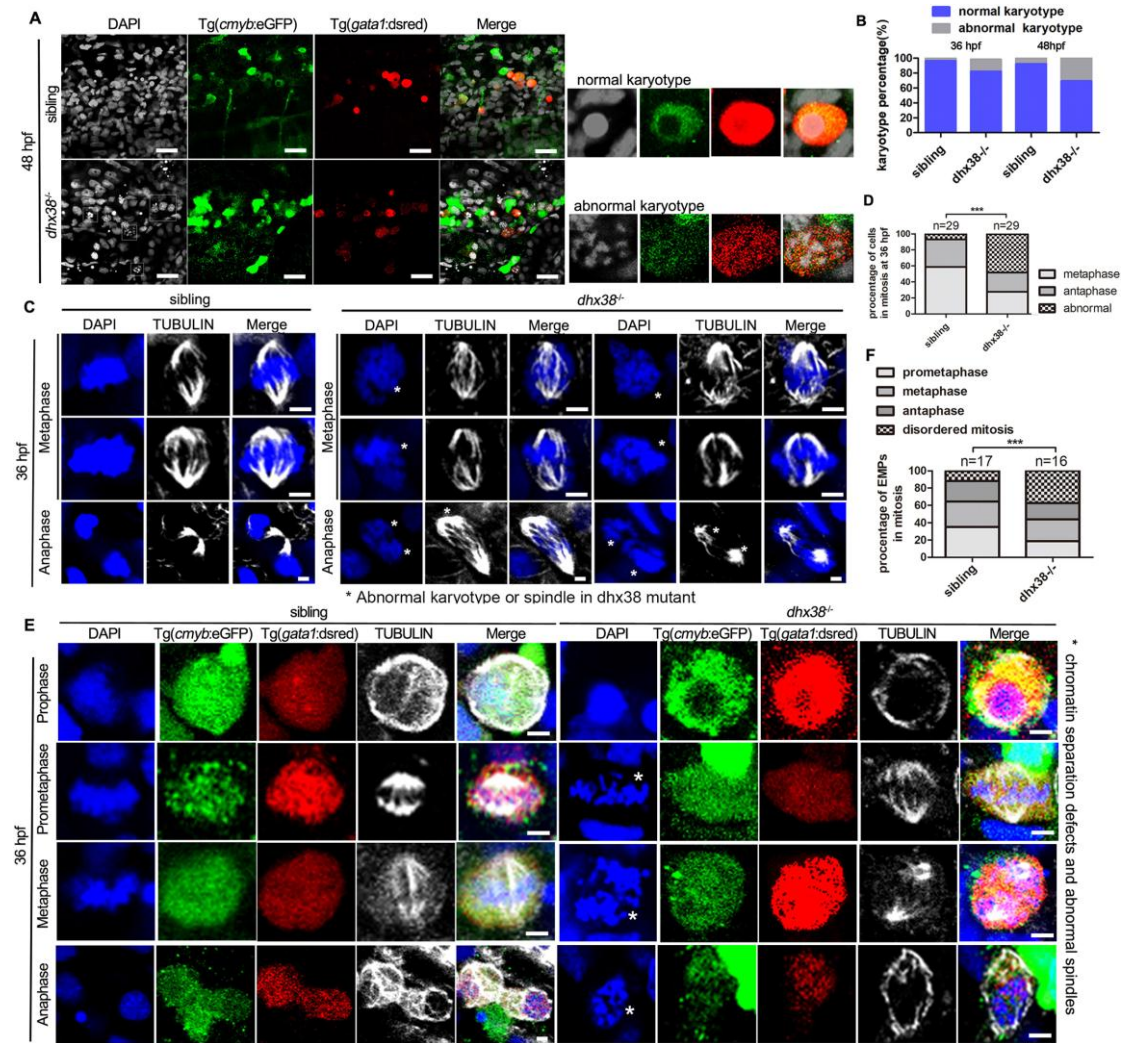
Fig. 5 EMPs in *dhx38* mutants exhibit disordered mitosis

A Confocal image of three-color immunostaining of Tg(*cmyb*:eGFP;*gata1*:dsred) fish and DAPI (white) reflect that an abnormal karyotype occurs in the *dhx38* mutants at 48 hpf. The grey boxes represent abnormal karyotypes. Scale bars, 50 μm. **B** The statistics of abnormal karyotype percentage from (A). 36 hpf number of abnormal karyotype: sibling, 32/768, *dhx38*^{-/-},128/820. 48 hpf number of abnormal karyotype: sibling, 64/736, *dhx38*^{-/-} ,248/552. **C** Confocal image of co-immunostaining for α-TUBULIN and DAPI. The first 3 panels in the Wildtype siblings show a normal karyotype and spindles during metaphase and anaphase. The last 6 panel in *dhx38*^{-/-} show a 'grape' karyotype in metaphase. The 'grape' karyotype appears to be chromosomes unable to align at the equatorial plate, and

progressing to disordered anaphase in *dhx38*^{-/-} embryo. Scale bars, 5 μm. **D** The statistics of double-positive fluorescence number from (C). **E** Confocal image of four-color immunostaining by *cmyb* (Gottgens et al.), *gata1* (red), DAPI (blue) and α-TUBULIN (white) at 36 hpf. EMPs (*cmyb*[+]*gata1*[+]) undergo normal prometaphase, metaphase and anaphase in siblings, but exhibit abnormal chromatin karyotype accompanied by a progressively abnormal spindle morphology in the *dhx38* mutants. Asterisks represent abnormal mitotic processes. Scale bars, 5 μm. **F** The statistics of EMP mitosis from (E).
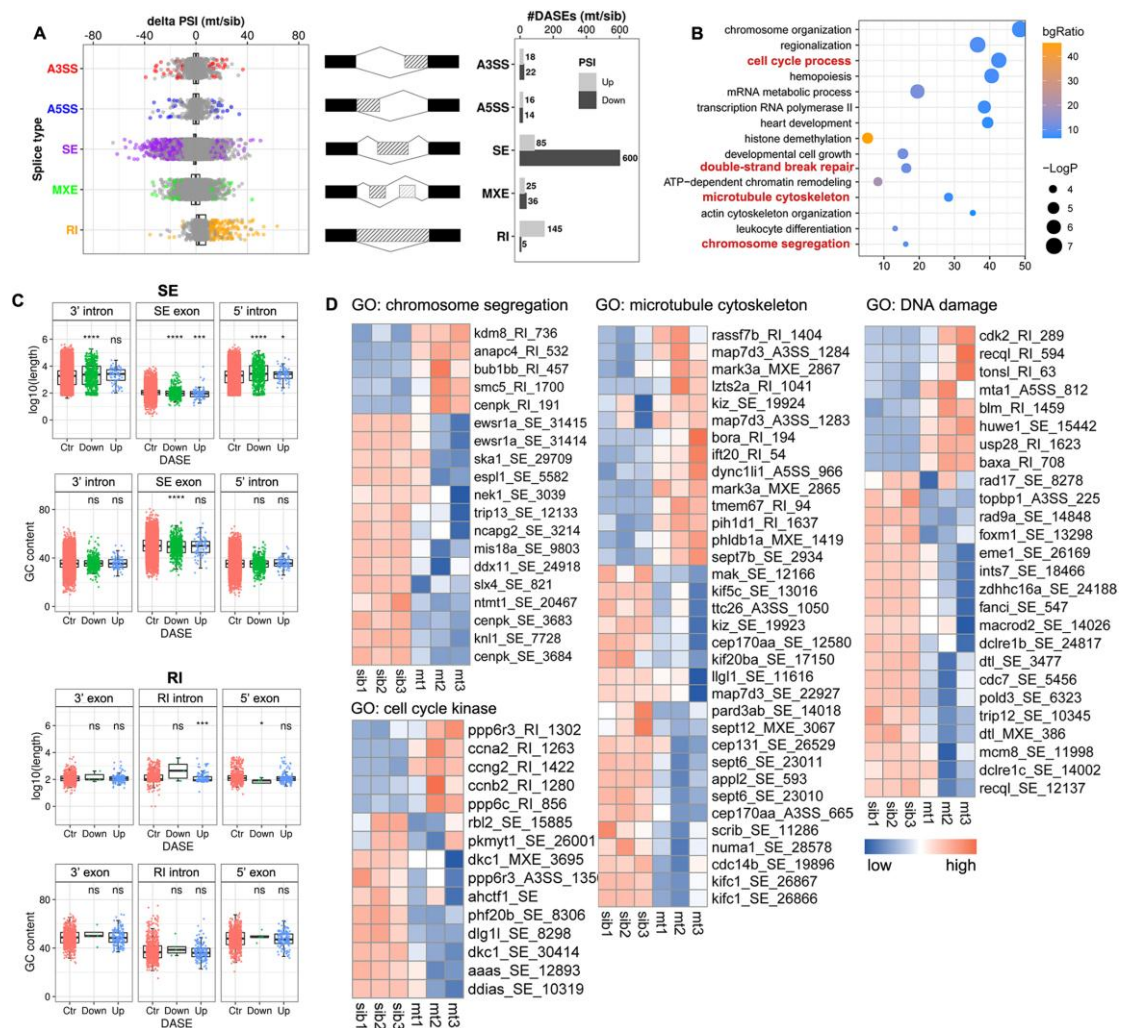
Fig. 6 Lack of *dhx38* results in abnormal alternative splicing in the cell cycle process.

A Categories of differential spliced genes based on the changed PSI value in the *dhx38* mutants. The percent spliced in index (PSI) indicates the efficiency of splicing a specific exon into the transcript population of a gene. Exons/intron that are constitutively retained in all transcripts and never skipped have a PSI of 100. So, the PSI UP indicate exon/intron that are more likely to be retained in the mutants and PSI DOWN are the exon/introns that more frequently skipped in the mutants. PSI, percent spliced in; A3SS, alternative 3' splice site; A5SS, alternative 5' splice site; SE, skipped exon; RI, retained intron; MXE, mutually exclusive exons. **B** GO enrichment of differentially spliced genes is significantly enriched in chromatin organization, microtubule cytoskeleton, cell cycle, and

Development • Accepted manuscript

DNA damage. **C** Sequence lengths and GC content around normal splicing sites and abnormal splicing sites in SE and RI events of *dhx38* mutants. In SE events, the length of PSI DOWN group of 3' and 5' introns is longer than the PSI control group, but the length of PSI UP group of introns in RI events is shorter. This suggests that longer introns in SE events and shorter introns in RI events are more likely to respond to the *dhx38* loss of function. The PSI DOWN group of GC content around the exon in differential SE events is lower in the *dhx38* mutants. This dmeonostartes that lower GC content of exons are more likely skipping when *dhx38* is knockedout. **D** Heat map of differentially spliced genes enriched in chromosome segregation, microtubule cytoskeleton, cell cycle kinase, and DNA damage.
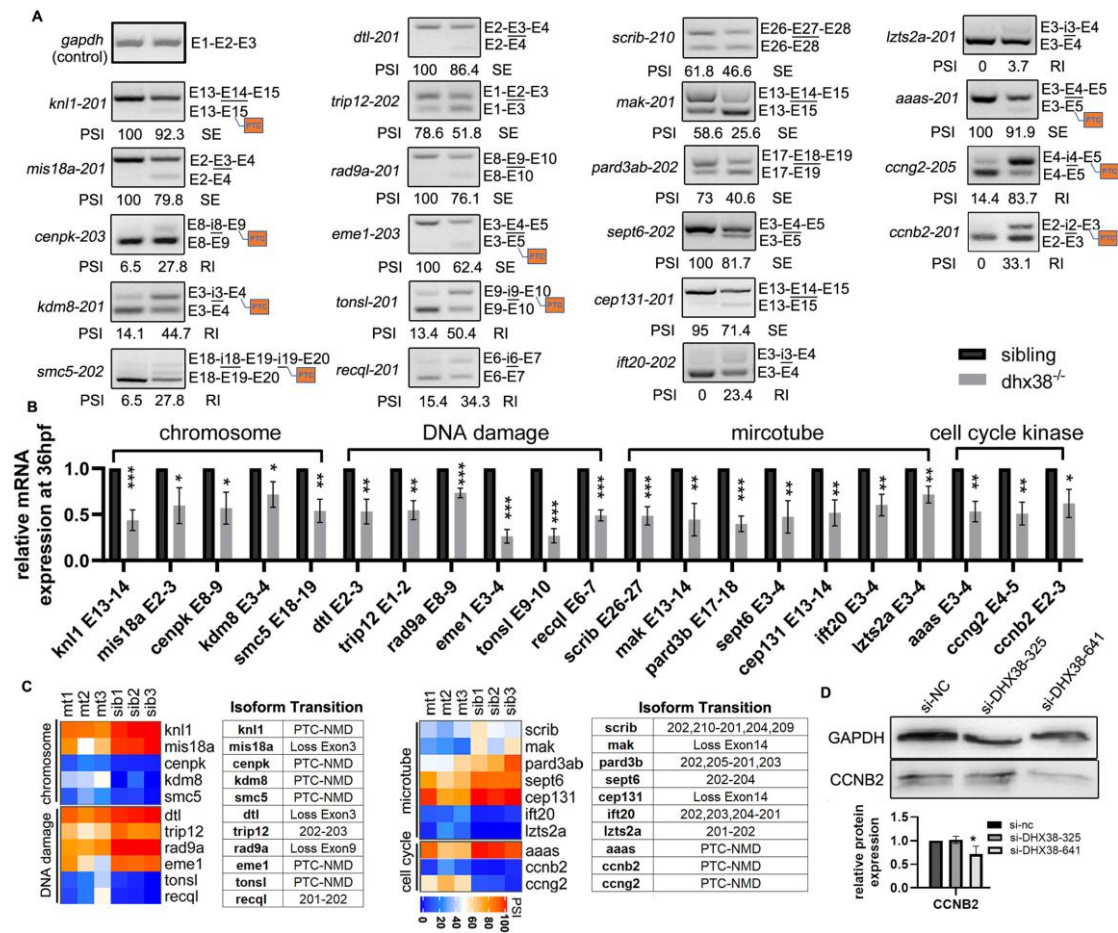
Fig. 7 DHX38 modulates the alternative splicing of a subset of genes involved in mitosis and DNA damage.

A Semi-qPCR confirms the abnormal splicing of the genes in Fig. 6D. The left band represents gene splicing in the wildtype siblings, while the right band represents splicing in the *dhx38* mutants. PSI, percent spliced in; A3SS, alternative 3' splice site; A5SS, alternative 5' splice site; SE, skipped exon; RI, retained intron; E, exon; i, intron; PTC, premature termination codon. Black line denotes abnormal spliced exon/intron. performed with three replicates; internal control, GAPDH. **B** qRT-PCR confirming mRNA expression of differentially spliced genes in (Fig. 6D). n ≥ 12 per group, performed with three replicates; internal control, GAPDH; two-tailed Student's t test, *p < 0.05, **p < 0.01, ***p < 0.001, ****p < 0.0001; error bars, mean ± SD. **C** The genes shown here are splicing abnormalities after being verified by semi-qPCR and their downregulate expression after

being confirmed by qRT-PCR. Of the genes assessed, *cenpk*, *smc5*, *knl1*, *kdm8*, *eme1*, *tonsl*, *ccng2*, *ccnb2* and *aaas* are predicted to undergo PTC-NMD events, while *trip12*, *scrib*, *pard3b*, *sept6*, *ift20*, and *lzts2a* undergo differential isoform transition, with *mis18a*, *dtl*, *rad9a*, *mak*, and *cep131* generating disordered isoform. **D** Western blot of CCNB2 in the si-DHX38-641 group displays decreased protein expression, compared to the si-nc or si-DHX38-325 group. n=3, *p=0.041.
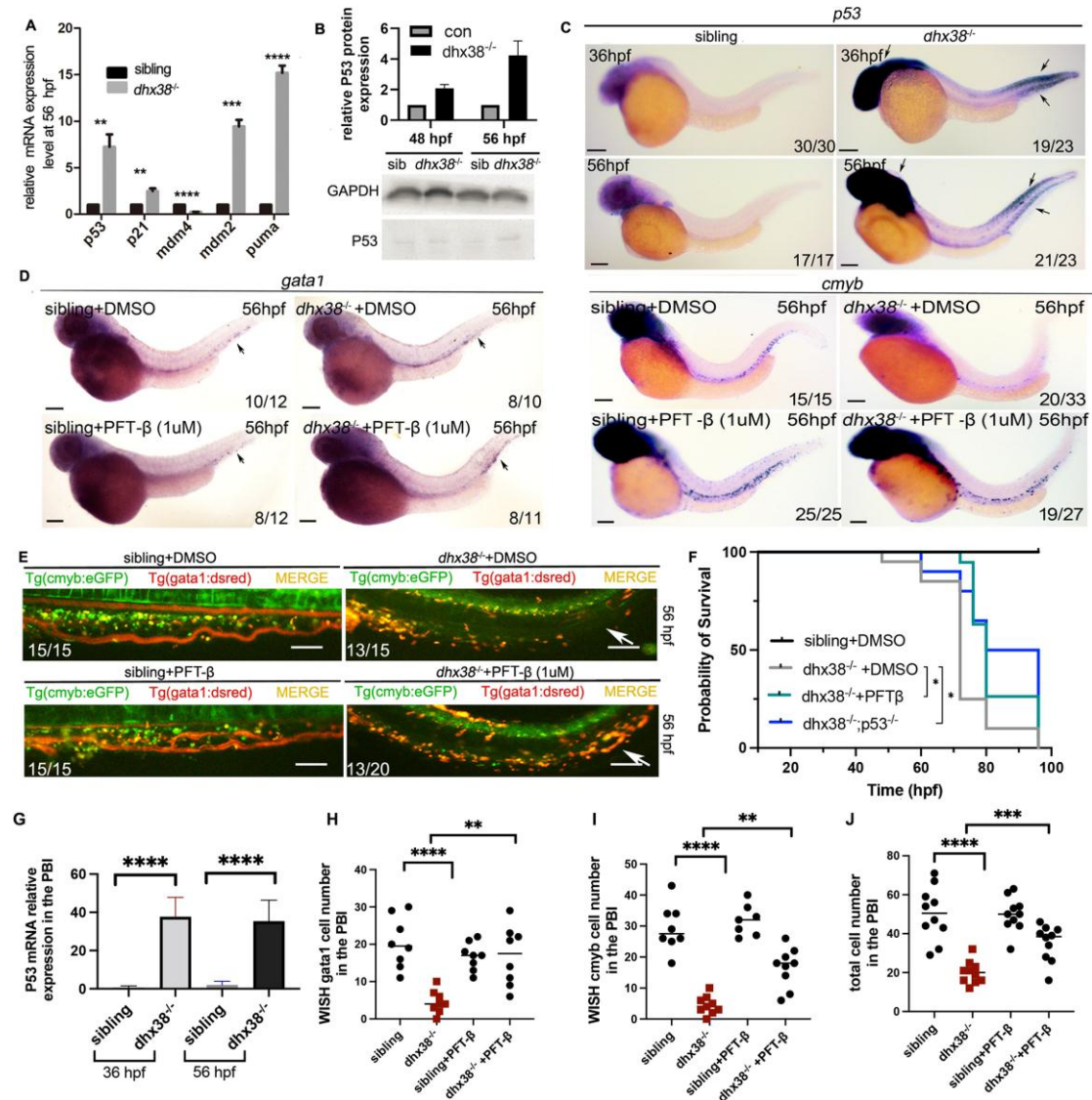
Fig. 8 EMPs and HSPCs in the *dhx38* mutants undergo *p53* dependent apoptosis.

A qRT-PCR of P53 signaling shows a significant increase in the expression of *p53*, *p21*, *puma* and *mdm2*. n ≥ 12 per group, performed with three replicates; internal control, GAPDH; two-tailed Student's t-test, *p < 0.05, **p < 0.01, ***p < 0.001, ****p < 0.0001; error bars, mean ± SD. **B** Western blot analysis shows an increased expression of P53 in *dhx38*⁻/⁻ zebrafish at 48 hpf, which increases further at 56 hpf. **C** The expression pattern of P53 detected by WISH reveals that P53 begins to accumulate in the PBI at 36 hpf and 48 hpf. Scale bars, 200 μm. **D** Decreased expression of *cmyb* and *gata1* in the *dhx38* mutants can be rescued following incubation with the P53 inhibitor PFT-β (1 uM). Scale

bars, 200 μm. **E** In vivo imaging of hematopoietic progenitor cells in Tg(*cmyb*:eGFP;*gata1*:dsred) at 56 hpf. The overall number of hematopoietic progenitor cells in the PFT-β group is higher than in the DMSO group. Scale bars, 200 μm. **F** The survival curve shows that PFT-β and *dhx38*$^{-/-}$;*p53*$^{-/-}$ rescue the survival rate of *dhx38* mutants. Compared with *dhx38*$^{-/-}$ embryo, the survival ratio of *dhx38*$^{-/-}$ incubated with PFT-β at 72 hpf (**p=0.003) and 76 hpf (*p=0.079) are significant. Compared with *dhx38*$^{-/-}$ embryo, the survival ratio of *dhx38*$^{-/-}$;*p53*$^{-/-}$ at 72 hpf (*p=0.012), 76 hpf (*p=0.029) and 80 hpf (**p=0.007) are significant. n ≥ 20 per group, performed with three replicates; two-tailed Student's t-test, error bars, mean ± SD. **G-J** Quantification of cells from (C-E), respectively; two-tailed Student's t-test; *p < 0.05, **p < 0.01, ***p < 0.001, ****p < 0.0001; error bars, mean ± SD.
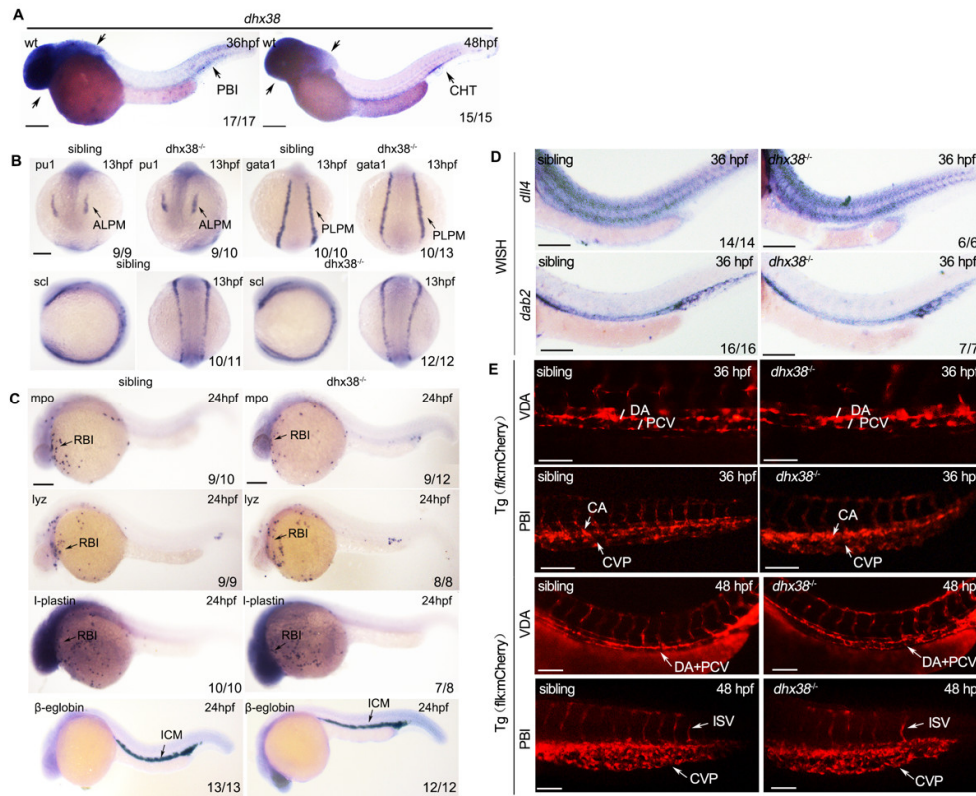
Fig. S1. Primary hematopoiesis and vascular development are unaffected in the *dhx38* mutants.

A WISH with a *dhx38* probe reflects *dhx38* expression in the PBI and CHT region at 36 hpf and 48 hpf, respectively. Black arrowheads indicate the expression pattern of *dhx38* markers. Scale bars, 200 µm. **B** Whole-mount in situ hybridization (WISH) was used to analyze the expression of the myeloid progenitor cell marker *pu.1*, the erythroid progenitor cell marker *gata1*, and the hemangioblastoma cells marker *scl* in siblings and *dhx38*$^{-/-}$ embryos at 13 hpf. Scale bars, 200 µm. **C** The expression of myeloid marker *mpo/lyz/l-plastin* at the rostral blood island (RBI) and erythroid marker *β-eglobin* at the intermediate cell mass (ICM) is normal in the *dhx38* mutants at 24 hpf. Scale bars, 200 µm. **D** WISH detected the expression of the arterial marker *dll4* and the vein marker *dab2* in the *dhx38*$^{-/-}$ embryo is identical to that of siblings. Scale bars, 100 µm. **E** Fluorescence observation of *flk*$^+$ endothelium in Tg(*flk*:mCherry) shows that vascular development is generally normal at 36 hpf and 48 hpf in the dhx38-/- embryos. DA: dorsal aorta, PCV: posterior cardinal vein, CA: caudal artery, CVP: caudal venous plexus, ISV: intersegmental vessels, white line: DA diameter. Scale bars, 50 µm.
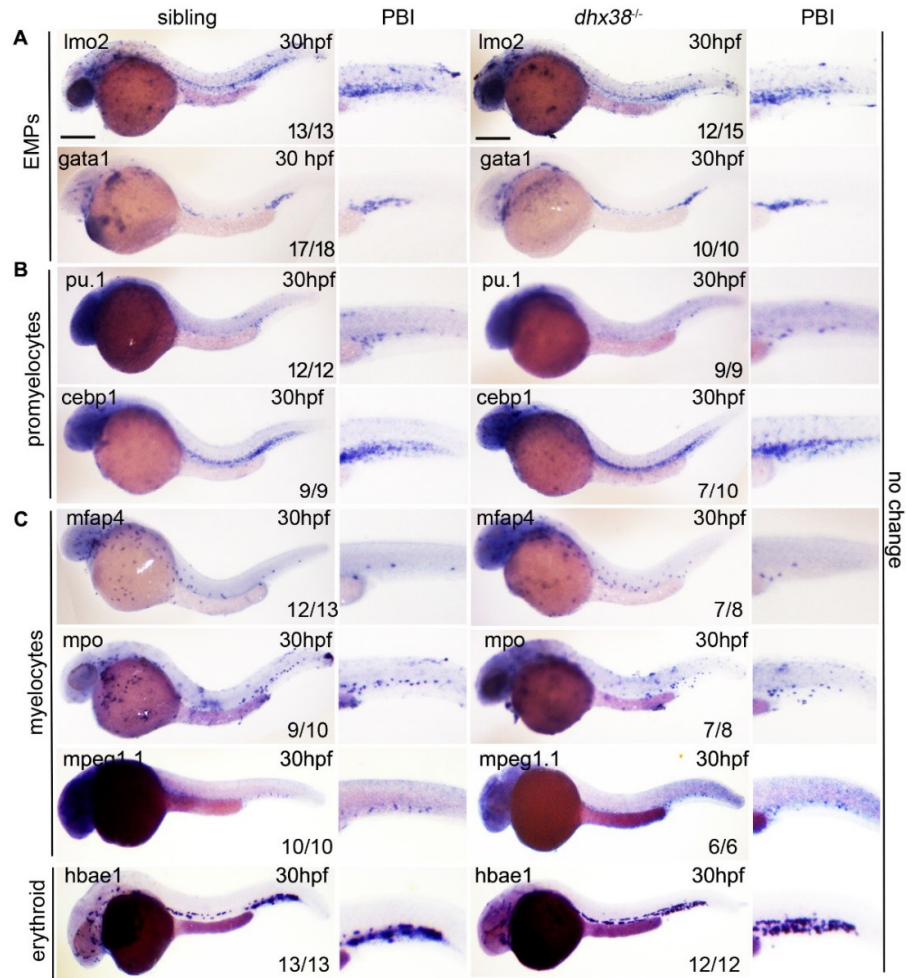
Fig. S2. EMP differentiation is normal in the *dhx38* mutant at 30hpf.

A, B WISH results with *lmo2*, *gata1*, *pu.1*, *cebp1*, *mfap4*, *mpo*, *mpeg1.1* and *hbae1* probes demonstrate that EMP development in *dhx38* mutant is identical to that of wild-type siblings. Scale bars, 200 μm.
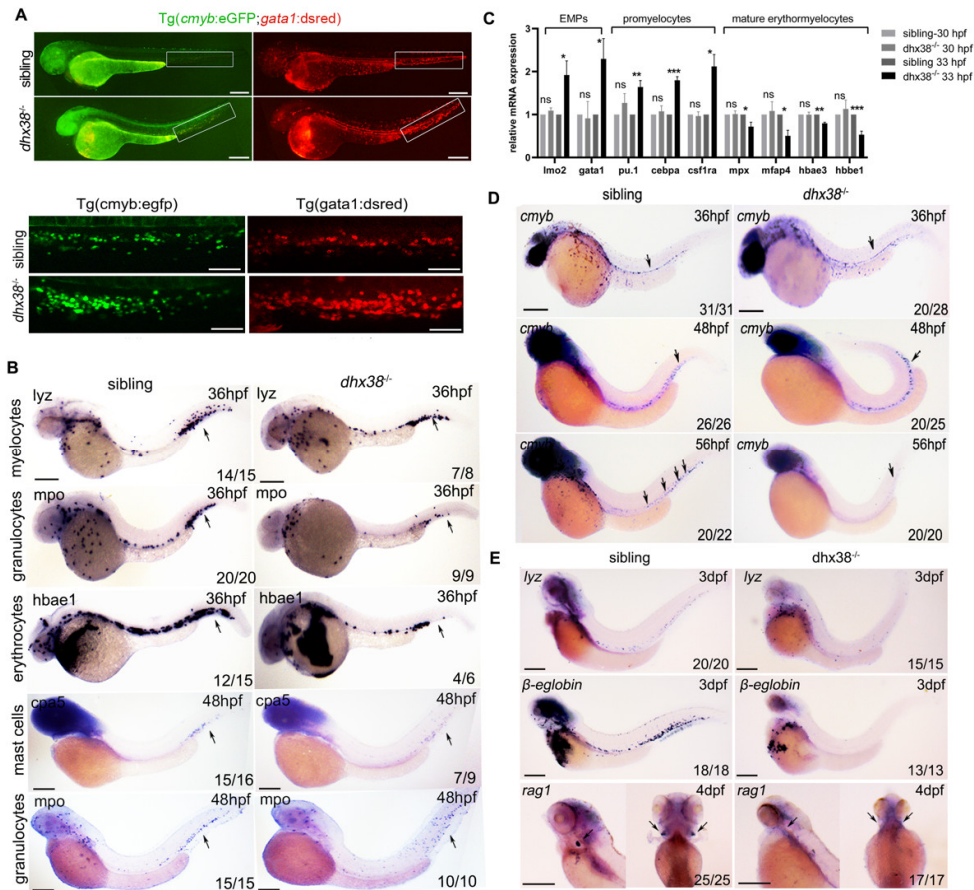
Fig. S3. Loss of *dhx38* impairs EMP differentiation.

A Whole embryo of Tg(*cmyb*:eGFP;*gata1*:dsred) shows increased EMPs at 36 hpf. Scale bars, 21 mm. With enlarged view in PBI region of the whole embryo. Scale bars, 50 μm. **B** WISH detected the expression of *lyz*, *mpo*, *hbae1* which are significantly decreased in *dhx38*⁻/⁻ zebrafish at 36 hpf. Scale bars, 200 μm. WISH detected the expression of *cpa5* and *mpo* showing that mature myeloid cells are decreased in *dhx38*⁻/⁻ zebrafish at 48 hpf. The black arrow indicated the CHT region of the zebrafish. Scale bars, 200 μm. **C** qRT-PCR analysis of genes related to EMP differentiation process in embryos at 30 hpf and 33 hpf. The EMPs specific genes *lmo2*, *gata1* and promyelocytes genes *pu.1*, *cebpa*, *csf1ra* are elevated, However mature erythromyelocyte marker genes (*mpx*, *mfap4*, *hbae3*, *hbae1*) are decreased at 33 hpf. n ≥ 12 per group, performed with three replicates; internal control, GAPDH; two-tailed Student's t-test, *p < 0.05, **p < 0.01, ***p < 0.001, ****p < 0.0001; error bars, mean ± SD. D The expression of the hematopoietic progenitor cell marker *cmyb* at 36 hpf, 48 hpf and 56 hpf in siblings and *dhx38* mutants. The black arrows indicate the position of the *cmyb* gene expression. Scale bars, 200 μm. E WISH analyzed the expression of the myeloid marker *lyz*, and the erythroid marker β-*eglobin*, and the lymphoid marker rag1 in dhx38 mutants and wild-type siblings. Black arrows indicated the position of marker gene expression. Scale bars, 200 μm.
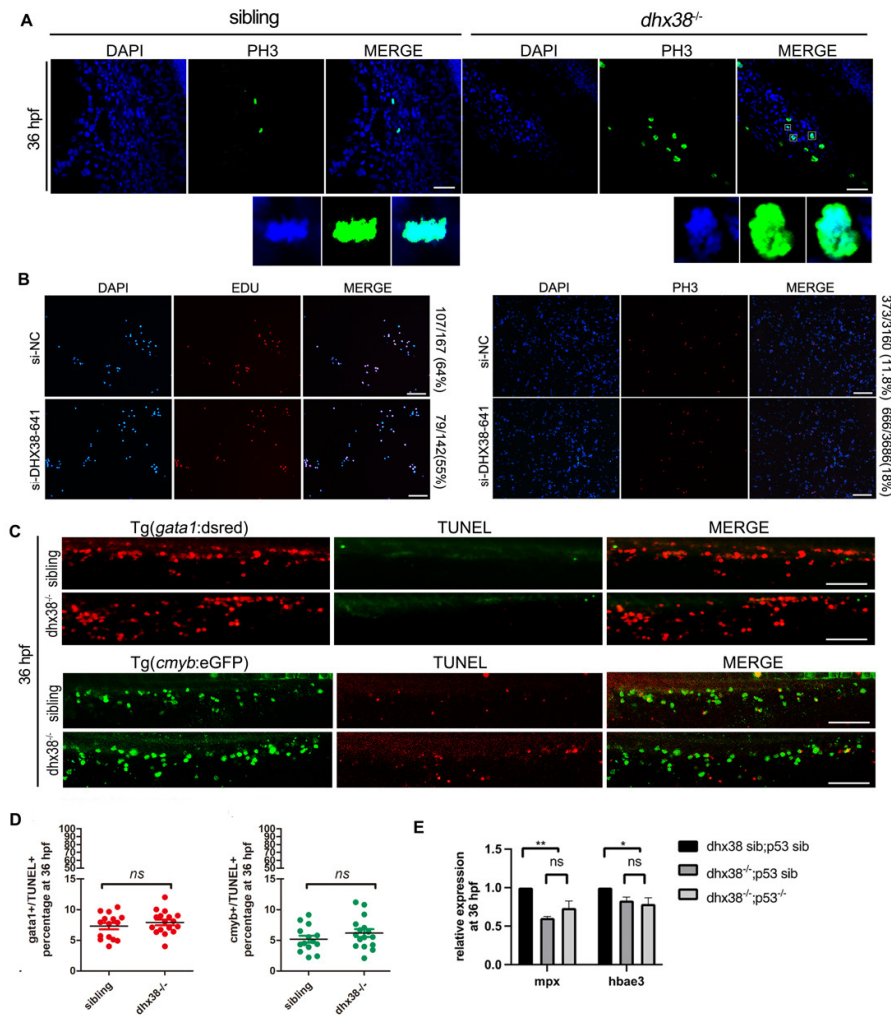
Fig. S4. *Dhx38* mutants exhibit disordered mitosis.

A Confocal image of immunostaining by DAPI and pH3 shows that pH3+ cells exhibit an abnormal karyotype in the *dhx38* mutants. Scale bars, 50 µm. **B** EdU assay shows a reduction of cells in S-phase from 64% to 55% in K562 cells following treatment with si-DHX38-641. Scale bars, 50 µm. pH3 immunostaining shows an increasement of cells in M- phase numbers from 11% to 18% in K562 cells following treatment with si-DHX38-641. Scale bars, 50 µm. **C** TUNEL staining shows that the proportion of apoptotic EMPs and HSPCs in *dhx38*⁻ᐟ⁻ embryos are identical to that of siblings at 36 hpf. **D** The double-positive fluorescence in the PBI show that EMPs and HSPCs are undergoing apoptosis. Scale bars, 100 µm. **E** Although p53 expression is increased in the mutants' CHT at 36 hpf, inhibiting *p53 activity in dhx38 mutants failed to rescue the phenotype of granulocyte (mpx) and 58 erythrocyte (hbae3) reduction at 36 hpf.*
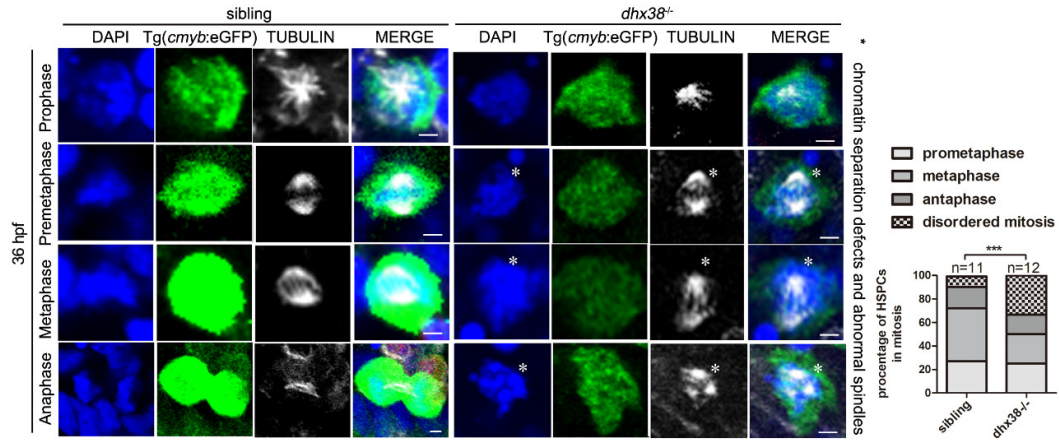
Fig. S5. HSPCs from *dhx38* mutants exhibit disordered mitosis.

Confocal image of three-color immunostaining by cmyb (green), DAPI (blue) and α-TUBULIN (white) at 36 hpf. HSPCs (*cmyb+*) from dhx38 mutants exhibiting disordered mitosis. Asterisks represents abnormal mitotic processes. Scale bars, 5 μm. The statistics of HSPC mitosis.
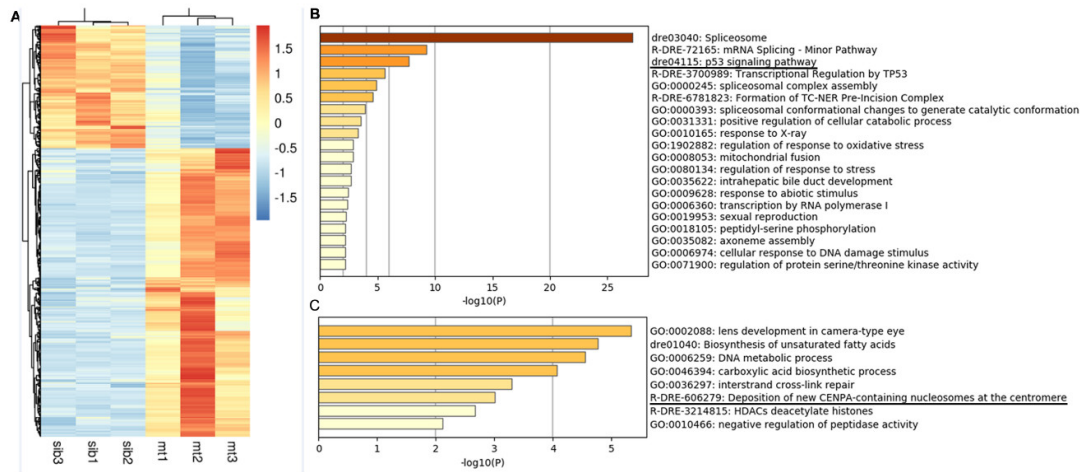
Fig. S6. Differentially expressed genes in the *dhx38* mutants.

A Heat map of differentially expressed genes. **B** GO enrichment map of up-regulated differentially expressed genes, black lines represent phenotypes associated with P53 signaling. **C** GO enrichment map of down-regulated differentially expressed genes, black lines represent phenotypes associated with chromosome segregation.
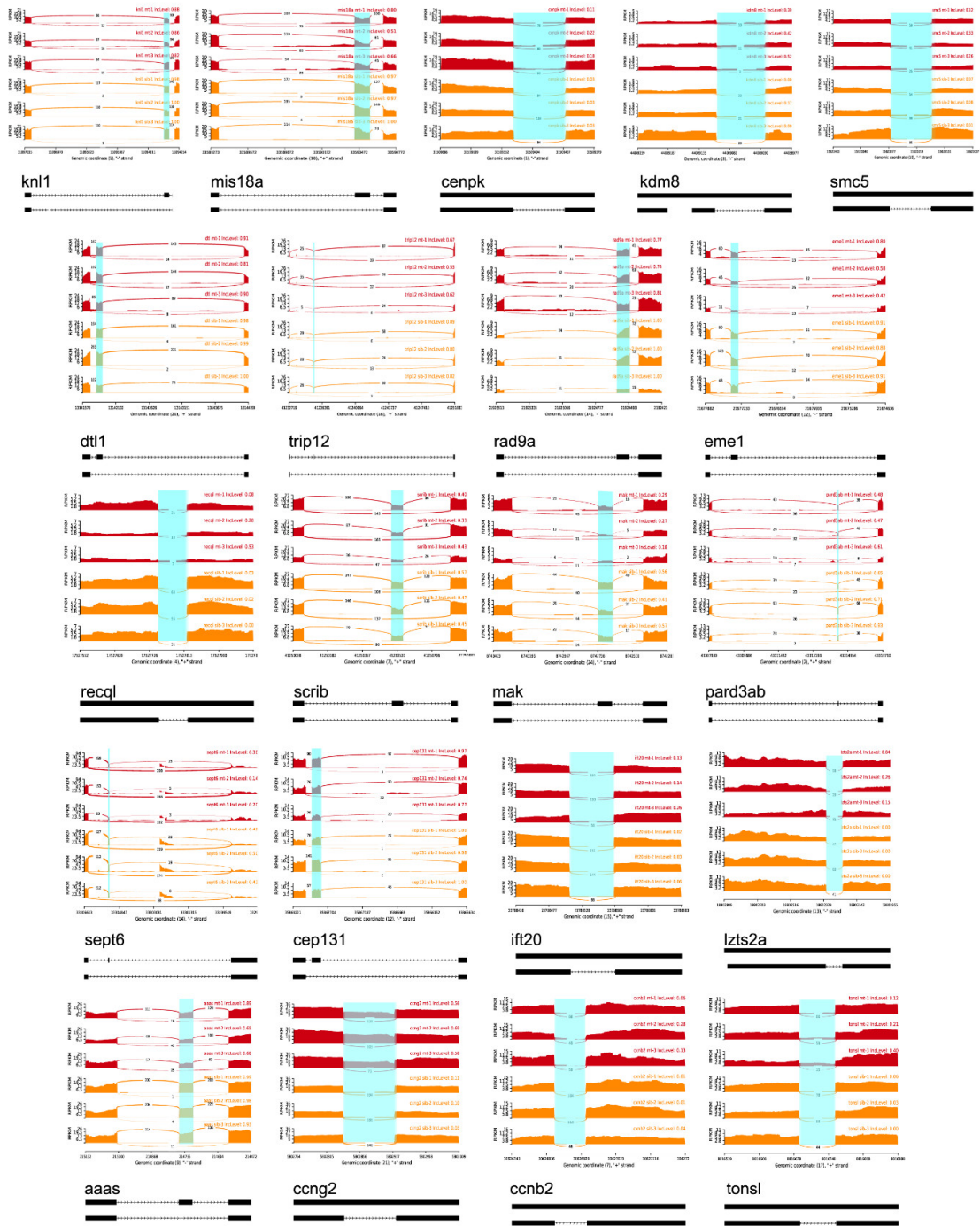
Fig. S7. Sahamiplot visualization of alternative splicing changes in selected genes in Fig 7.

Junction reads and IncLevels were assessed by IGV to further confirm the presence of selected differential spilced genes in Fig 7 between wild-type sibling and *dhx38* mutants.
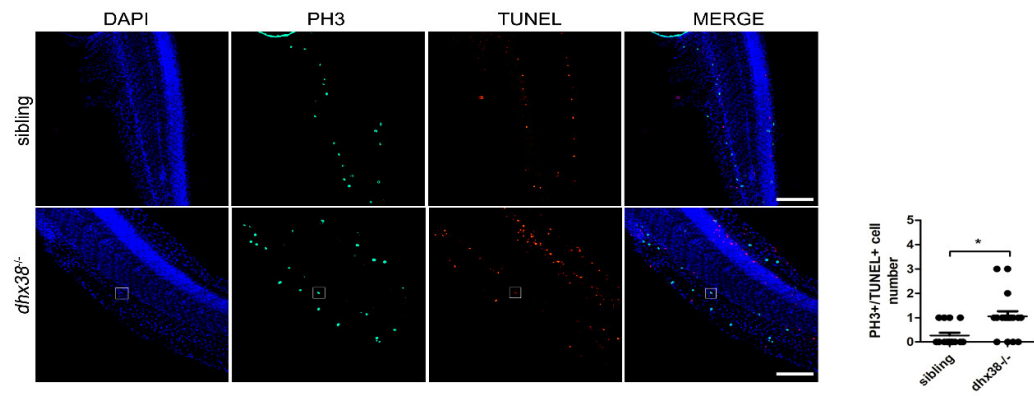
Fig. S8. Impaired mitosis and activated apoptosis in the *dhx38* mutants.

Confocal image of immunostaining by TUNEL and pH3 shows co-localization of pH3
[+] cells and TUNEL^{+} cells in the *dhx38^{-/-}* zebrafish at 56 hpf. Scale bars, 50 μm. The
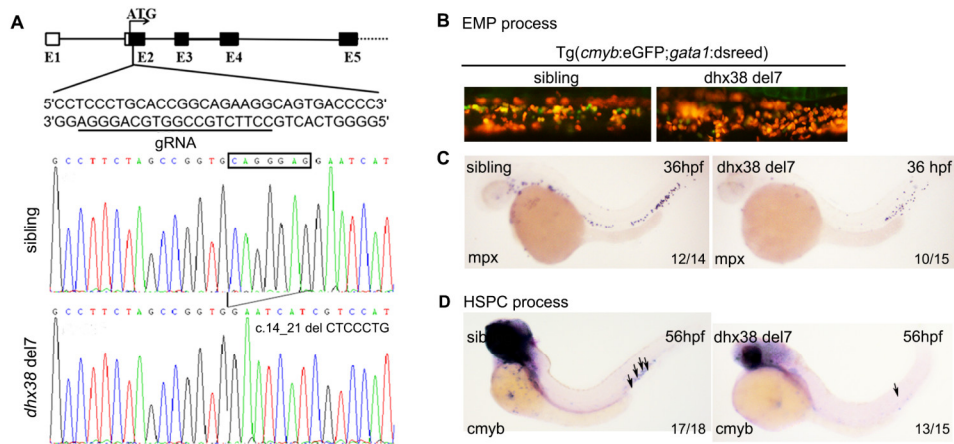statistics of cells exhibiting co-localization.

Fig S9. Enhanced EMP progenitor and impaired HSPC maintenance in *dhx38* del 7 mutants.

A A schematic diagram of the *dhx38* gRNA locus. DNA sequencing identified a 7 bp deletion of cDNA (c.14_21delCTCCCTG), which predicts a truncated protein (p.Ser5_ThrfsTer8). **B** In vivo imaging of EMPs and HSPCs in the PBI region of Tg(*cmyb*:eGFP;*gata1*:dsred) fish at 36 hpf. The number of EMPs and HSPCs in the *dhx38*$^{-/-}$ zebrafish is higher than that in wild-type siblings. **C** WISH results reflecting the expression of mature myelocytes (*mpx*) is decreased in the *dhx38* del7 mutant at 36 hpf. **D** The expression of the hematopoietic progenitor cells marker *cmyb* at 56 hpf in siblings and *dhx38* del7 mutants. The black arrows indicate the position of the *cmyb* gene expression.

Table S1. Significant differential expression genes in the *dhx38* mutants.

Click here to download Table S1

Table S2. GO enrichment of significant differential expression genes in Supplemental Table S1.

Click here to download Table S2

Table S3. All significant differential alternative spliced events in the *dhx38* mutants and the predicted of gene transcript swift after differential spliced.

Click here to download Table S3

Table S4. All significant differential spliced genes, GO enrichment of differential splicing genes.

Click here to download Table S4

Table S5. All Primers used in this study. Including semi-PCR, qRT-PCR, identified of dhx38 genotype primers, and WISH probe primers.

Click here to download Table S5

Table S6. Antibodies used in this study

Antibodies	Source	Cat#	RRID	Dilution
Anti-α-Tubulin	GeneTex	GTX76511	AB_378784	1:100 for IF
Anti-pH3	Affinity	AF3358	AB_2834773	1:200 for IF
Anti-GFP	Dai-an	2057	N.A.	1:200 for IF
Anti-mcherry	Affinity	T0090	AB_2843441	1:200 for IF
DAPI	Thermo Fisher Scientific	D1306	AB_2629482	1:1000 for IF
Goat anti-Rabbit IgG (H+L) Secondary Antibody, Alexa Fluor 594	Thermo Fisher Scientific	A-11012	AB_2534079	1:1000 for IF
Goat anti-Rabbit IgG (H+L) Secondary Antibody, Alexa Fluor 488	Thermo Fisher Scientific	A-31565	AB_2536178	1:1000 for IF
Goat anti-Mouse IgG (H+L) Secondary Antibody, Alexa Fluor 488	Thermo Fisher Scientific	A-11001	AB_2534069	1:1000 for IF
Goat anti-Mouse IgG (H+L) Secondary Antibody, Alexa Fluor 594	Thermo Fisher Scientific	A-11005	AB_2534073	1:1000 for IF
Goat anti-Rat IgG (H+L) Secondary Antibody, Alexa Fluor 647	Thermo Fisher Scientific	A-21247	AB_141778	1:1000 for IF
Anti-P53	GeneTex	GTX128135	AB_2864277	1:500 for WB
Anti-GAPDH	Dia-an	2058	N.A.	1:500 for WB
Goat anti-Rabbit IgG (H+L) Secondary Antibody, HRP	Thermo Fisher Scientific	31460	AB_228341	1:20000 for WB
Goat anti-Mouse IgG (H+L) Secondary Antibody, HRP	Thermo Fisher Scientific	31430	AB_228307	1:20000 for WB
Anti-DHX38	Proteintech	10098-2-AP	AB_2092294	1:1000 for WB
Phospho-Histone H2A.X (Ser139) Antibody	Cell Signaling Technology	2577	AB_2118010	1:1000 for WB
Anti-SMC5	Proteintech	14178-1-AP	AB_2192775	1:1000 for WB
Anti-CCNB2	Thermo Fisher Scientific	PA5-86965	AB_2803721	1:1000 for WB

Table S7. the sequence of siRNA used in this study

siRNA	Sequence	
Negative control (Nc)	5'-3'	UUCUCCGAACGUGUCACGUTT
	3'-5'	ACGUGACACGUUCGGAGAATT
DHX38-Homo-641	5'-3'	GCGGGAACAUGGUGUCUAUTT
	3'-5'	AUAGACACCAUGUUCCCGCTT
DHX38-Homo-325	5'-3'	GCGAGCAGCAUGUCUUCAATT
	3'-5'	UUGAAGACAUGCUGCUCGCTT